HHS Public Access

Author manuscript

Cell Rep. Author manuscript; available in PMC 2023 January 05.

Published in final edited form as:

Cell Rep. 2022 November 29; 41(9): 111726. doi:10.1016/j.celrep.2022.111726.

The ribosomal RNA processing 1B:protein phosphatase 1 holoenzyme reveals non-canonical PP1 interaction motifs

Gautam Srivastava[1], **Rakhi Bajaj**[2], **Ganesan Senthil Kumar**[1,3], **Antoine Gaudreau-Lapierre**[4,5], **Hannah Nicolas**[4,5], **Delphine Chamousset**[4,5], **Dale Kreitler**[6], **Wolfgang Peti**[1], **Laura Trinkle-Mulcahy**[4,5,*], **Rebecca Page**[7,8,*]

[1]Department of Molecular Biology and Biophysics, UConn Health, Farmington, CT 06030, USA

[2]Department of Molecular Biology, Cell Biology and Biochemistry, Brown University, Providence, RI 02912, USA

[3]Integrative Structural Biology Laboratory, National Institute of Immunology, Aruna Asaf Ali Marg, New Delhi 110067, India

[4]Department of Cellular and Molecular Medicine, University of Ottawa, Ottawa, ON K1H 8M5, Canada

[5]Ottawa Institute of Systems Biology, University of Ottawa, Ottawa, ON K1H 8M5, Canada

[6]Brookhaven National Laboratory, National Synchrotron Light Source II, Upton, NY 11973, USA

[7]Department of Cell Biology, UConn Health, Farmington, CT 06030, USA

[8]Lead contact

SUMMARY

The serine/threonine protein phosphatase 1 (PP1) dephosphorylates hundreds of substrates by associating with >200 regulatory proteins to form specific holoenzymes. The major PP1 targeting protein in the nucleolus is RRP1B (ribosomal RNA processing 1B). In addition to selectively recruiting PP1β/PP1γ to the nucleolus, RRP1B also has a key role in ribosome biogenesis, among other functions. How RRP1B binds PP1 and regulates nucleolar phosphorylation signaling is not yet known. Here, we show that RRP1B recruits PP1 via established (RVxF/SILK/ΦΦ) and non-canonical motifs. These atypical interaction sites, the PP1β/γ specificity, and N-terminal AF-binding pockets rely on hydrophobic interactions that contribute to binding and, via

*Correspondence: ltrinkle@uottawa.ca (L.T.-M.), rpage@uchc.edu (R.P.).

AUTHOR CONTRIBUTIONS

R.P., L.T.-M., and W.P. developed the concept. R.B., G.S.K., and G.S. expressed and purified all proteins. R.B. and G.S.K. performed NMR and ITC experiments and initial crystallization trials and analyzed data. G.S. performed and optimized crystallization experiments and completed final structure determination, and performed SPR experiments. D.K. processed and phased initial crystallographic data. A.G.-L., H.N., and D.C. created variants for cellular experiments and performed immunoprecipitation/western blotting and imaging experiments. L.T.-M. performed the fluorescence two-hybrid screen and analyzed data. R.P. and W.P. wrote the manuscript with comments and input from all co-authors.

DECLARATION OF INTERESTS

The authors declare no competing interests.

SUPPLEMENTAL INFORMATION

Supplemental information can be found online at https://doi.org/10.1016/j.celrep.2022.111726.

phosphorylation, regulate complex formation. This work advances our understanding of PP1 isoform selectivity, reveals key roles of N-terminal PP1 residues in regulator binding, and suggests that additional PP1 interaction sites have yet to be identified, all of which are necessary for a systems biology understanding of PP1 function.

In brief

Srivistava et al. determine the structure of the RRP1B:PP1 holoenzyme complex. In addition to identifying the molecular basis of PP1 isoform selectivity, they show how phosphorylation outside the RRP1B RVxF motif regulates holoenzyme assembly. This work advances our understanding of the PP1 regulatory code, essential for Ser/Thr dephosphorylation signaling.

Graphical Abstract

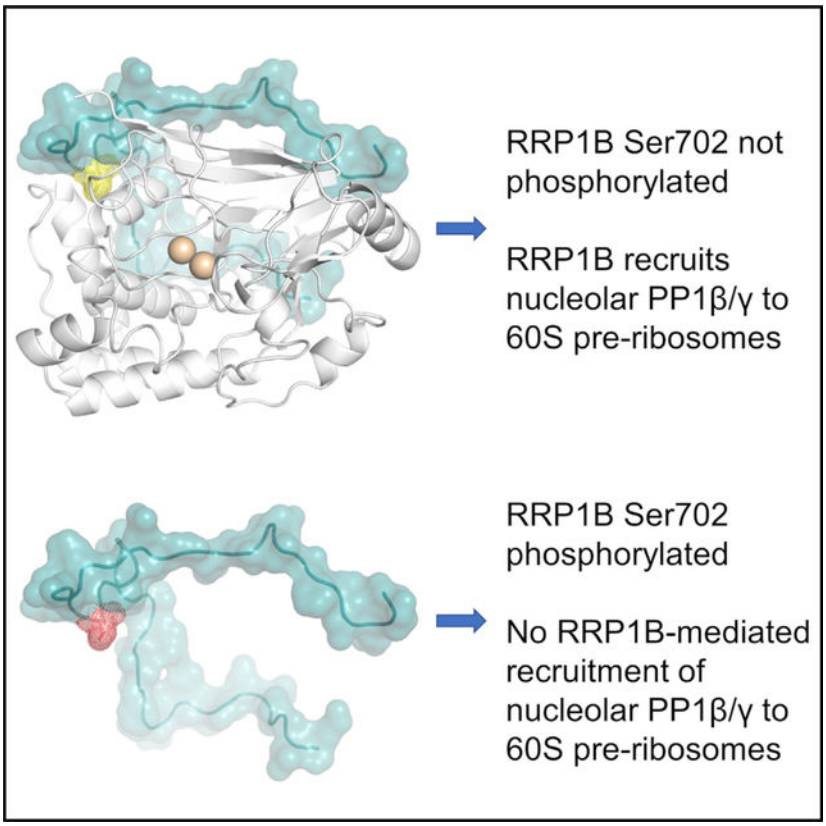

INTRODUCTION

Protein phosphatase 1 (PP1) is one of the most widely expressed and abundant serine/threonine phosphatases.[1] Highly conserved from fungi to humans, dephosphorylation events mediated by PP1 regulate processes as diverse as cell-cycle progression to neuronal signaling, with PP1 dysregulation resulting in disease, such as drug addiction and cancer.[2] PP1 achieves specificity by interacting with >200 known regulatory proteins.[3,4] These regulators target PP1 to distinct cellular compartments and direct its activity toward specific substrates.[5] Although it was discovered more than 30 years ago that most regulators bind

PP1 via the RVxF short linear motif (SLiM),[6,7] many studies have shown that regulator binding is typically much more complex, with regulators using additional motifs beyond the RVxF SLiM for PP1 holoenzyme formation.[8–13] While the extent and complexity of these interactions are providing insights into PP1 biology, many open questions remain. For example, are there additional interaction sites to be identified, how do regulators distinguish between the highly conserved PP1 isoforms (PP1α, PP1β, and PP1γ), how are regulator-PP1 interactions regulated by post-translational modification, and how do these interactions impact PP1-regulated biological processes?

One cellular compartment that is selectively populated by specific PP1 isoforms is the nucleolus.[14,15] While the most established function of the nucleolus is ribosome biogenesis, recent studies have demonstrated that it plays critical roles in other cellular processes, including the stress response, ribonucleoprotein complex assembly, RNA processing, and mitosis, among others.[16,17] These nucleolar functions are regulated by phosphorylation events catalyzed by nucleolar-specific kinases and phosphatases.[18] Our previous effort to define the nucleolar phosphatome showed that PP1 accounts for ~80% of the Ser/Thr phosphatase activity in the nucleolus and that this activity is due to the selective nucleolar localization of only two of the three mammalian PP1 isoforms, PP1β and PP1γ.[19] We also determined, by quantitative affinity purification-mass spectrometry, that the PP1 regulatory subunit most enriched in a pull-down of the catalytic subunit is the ribosomal RNA processing 1 homolog b protein (RRP1B; KIAA0179; 758 amino acids; 84.4 kDa).[15] It is the selective interaction of RRP1B with PP1β and PP1γ that results in the accumulation of only these PP1 isoforms, but not PP1α, in the nucleolus.

RRP1B is the second human isoform of the yeast Rrp1p protein, a component of the yeast 66S pre-ribosome that precedes the production of the yeast 60S ribosomal subunit.[20] While both human homologs of Rrp1p (RRP1 and RRP1B) contain the N-terminal nucleolar protein 52 kDa (NOP52/RRP1/NNP-1) domain that mediates pre-ribosome binding, the intrinsically disordered C termini (IDRs) of both homologs differ considerably, with that of RRP1B being ~300 amino acids longer. Thus, although it had been assumed that RRP1B was the functional ortholog of Rrp1p, the emerging view is that this role is primarily fulfilled by RRP1 with RRP1B largely performing other functions due mainly to its extensive, dynamic C terminus. Consistent with this view, RRP1B was recently identified as a metastasis modifier gene in breast cancer, with differential RRP1B expression predicting breast cancer-specific survival.[21,22] Subsequent studies revealed that RRP1B also plays a role in cellular proliferation, transcription regulation, mRNA splicing, chromatin modulation, ribosome biogenesis, and, via PP1 binding, phosphorylation signaling.[15,22–24] However, how RRP1B binds and recruits PP1, how this recruitment is isoform specific, and if and how these interactions direct PP1 activity toward specific substrates in the nucleolus remain open questions.

Here, we combine structural, biochemical, and cellular studies to define how RRP1B recruits PP1 to the nucleolus. We show that the PP1-binding domain of RRP1B extends beyond its RVxF motif, spanning >50 amino acids. Specifically, RRP1B binds PP1 via multiple regulator binding pockets, including sites not previously shown to bind to any PP1 regulator. This led to the identification of an atypical regulator interaction pocket on

PP1, which we have named the AF-binding pocket. We also discovered that RRP1B uses a non-canonical SILK motif to bind the PP1 SILK interaction pocket. This not only expands the experimental definition of the SILK SLiM, but also shows that the SILK interaction is clearly much more prominent in the regulation of PP1 than previously assumed. Finally, we also show why RRP1B selectively binds and recruits only the β and γ isoforms of PP1 and how the RRP1B-mediated recruitment of PP1 is likely regulated by phosphorylation. Together, these data show how the discovery of additional regulatory interaction sites on PP1 not only provides key insights into the mechanisms by which regulators direct the subcellular distribution and activity of PP1 but also offers additional targets for the selective disruption of distinct PP1 holoenzymes.

RESULTS

The isoform selectivity of RRP1B for PP1β and PP1γ is determined by a single amino acid

In cells, RRP1B binds to the β and γ isoforms (PP1β, PP1γ), but not the α isoform, of PP1 (PP1α) to exclusively form PP1β:RRP1B and PP1γ:RRP1B holoenzymes (constructs used in this study are illustrated in Figures 1A and 1B).[15] We confirmed this *in vitro* using isothermal calorimetry (ITC), which showed that the binding affinity of $RRP1B_{657–758}$ for PP1α is more than 22-fold weaker than that of PP1γ (K_D = 888 ± 113 nM versus 40 ± 8 nM for PP1α and PP1γ, respectively; Figures 2A and 2B; Table S1). To determine the molecular basis of isoform specificity of RRP1B for PP1γ, we first tested the role of the PP1α and PP1γ C-terminal residues (most of the primary sequence differences between PP1α and PP1γ are in the C-terminal ~25-amino-acid disordered tail, while only seven residues differ in the folded, PP1 catalytic domain [Figure 1B]). Deleting the PP1γ C-terminal tail did not impact RRP1B binding *in vitro* (K_D = 17.6 ± 1 nM; Figure S1 and Table S1). We confirmed this result in cells using fluorescence imaging and pull-down assays. As expected, when GFP is fused to PP1γ, a pool accumulates in the nucleolus (Figure 2C, top panels). However, neither deleting the PP1γ C-terminal residues (PP1γ-ΔC, Figures 1B and 2C [bottom left panel]) nor replacing them with the C-terminal tail from PP1α (PP1γ-αC, Figures 1B and 2C [bottom right panel]) altered this nucleolar localization. Consistent with this, GFP-trap pull-down assays show that RRP1B binds equally well to PP1γ, PP1γ-ΔC, and PP1γ-αC (Figure 2D; compare with apoptosis-stimulating protein of p53 [ASPP2], a PP1-specific regulator that we and others previously showed to require the PP1 C-terminal tail for binding[12,25]).

Together, these data demonstrate that the observed isoform specificity of RRP1B for PP1γ is not due to the C-terminal tail but instead is due to one or more of the seven amino acids that differ in the catalytic domains of PP1α and PP1γ (Figure 1B). This suggested that RRP1B may bind PP1γ in a manner leveraged by two other PP1γ-specific regulators: RepoMan and Ki-67.[11] This is because while the sequence of RRP1B differs significantly from that of RepoMan and Ki-67, like RRP1B, RepoMan and Ki-67 do not require the C-terminal residues of PP1γ for binding and selectivity. Previously, we showed that the isoform specificity of RepoMan and Ki-67 is due to a single amino acid difference in PP1 at position 20, which is an Arg residue in PP1γ/β and a Gln residue in PP1α. To determine whether PP1 residue 20 also defines the isoform selectivity of RRP1B, we measured the

binding affinity of RRP1B for a mutant of PP1α in which residue 20 was changed to that present in PP1γ, PP1α Q20R (Figure 2E). This single amino acid change resulted in a ~14-fold increase in affinity, resulting in a K_D nearly identical to that of wild-type (WT) PP1γ (PP1α Q20R, 64 nM versus PP1γ, 40 nM), confirming the key role of PP1 residue 20 for RRP1B binding. We confirmed this result in live cells expressing GFP-tagged WT and mutant constructs. While the WT PP1α is distributed throughout the cytoplasm and nucleoplasm (Figure 2F, upper left panel), the PP1α Q20R mutant shows an additional accumulation in nucleoli, similar to that observed for WT PP1γ (Figure 2F, upper right and lower left panels). Likewise, generating the reverse mutation in PP1γ (R20Q) significantly reduced its nucleolar localization (Figure 2G, lower right panel). This is consistent with a study, published several years prior to our identification of RRP1B as a PP1 regulatory subunit, which linked this residue to nucleolar recruitment.[26] We have now confirmed by GFP-trap pull-down assays that the R20Q mutation in PP1γ abrogates RRP1B binding to an extent similar to that observed for RepoMan, while the Q20R mutation in PP1α confers the ability to bind both (Figure 2G). Together, these data show that a single amino acid in PP1γ, R20, is responsible for the enhanced affinity of RRP1B for PP1γ and, in turn, its RRP1B-mediated recruitment to the nucleolus.

The RRP1B PP1 interaction domain extends beyond the RVxF SLiM

Although the amino acid sequence of RRP1B differs significantly from that of RepoMan and Ki-67, the shared mechanism of isoform selectivity suggests they may share common elements of PP1 binding. We and others have shown that while most PP1 regulators contain RVxF SLiMs, they often interact with PP1 via additional residues.[8,10,11] To identify the full RRP1B PP1-binding domain, we used biomolecular nuclear magnetic resonance (NMR) spectroscopy. In agreement with the prediction by IUPRED,[27] a program that predicts the presence of intrinsically disordered proteins and regions (IDPs/IDRs) using primary sequence, the two-dimensional (2D) [^{1}H,^{15}N] heteronuclear single quantum coherence (HSQC) spectrum of ^{15}N-labeled $RRP1B_{657–758}$ exhibits all hallmarks of an IDP, including narrow chemical shift dispersion in the ^{1}H dimension due to the lack of hydrogen bonds in secondary structure elements (Figure 3A). After completing the sequence-specific backbone assignment of $RRP1B_{657–758}$, a secondary structure propensity (SSP[28]) analysis using Cα and Cβ chemical shifts confirmed that $RRP1B_{657–758}$ does not have any significant preferred secondary structures (Figure S2). To define the full RRP1B PP1-binding domain, we measured a 2D [^{1}H,^{15}N] HSQC spectrum of ^{15}N-labeled RRP1B bound to $PP1\gamma_{7–308}$. In this experiment, the cross-peaks corresponding to residues that bind PP1 disappear due to the increased molecular weight of the RRP1B:PP1 complex (~45 kDa), while the peaks corresponding to residues that do not bind remain visible.[10,11,29,30] Overlaying the free and PP1-bound spectra showed that the minimal RRP1B PP1-binding domain is contained within RRP1B residues 677–736, as the cross-peaks corresponding to the central residues disappeared upon complex formation while those at the boundaries (677–680, 732–736) showed significantly reduced intensities (Figures 3A and 3B). This was confirmed using ITC, which showed that the binding affinity of $RRP1B_{677–736}$ with $PP1\gamma_{7–308}$ (K_D = 22.6 ± 6 nM) was essentially identical to that of $RRP1B_{657–758}$ (Figure 3C and Table S1). These data show that $RRP1B_{677–736}$ not only extends far beyond the ^{683}KVTF^{686} PP1-specific SLiM but is also ~20 amino acids longer than the PP1 interaction domain of RepoMan/

Ki-67, suggesting that while they likely both bind directly to PP1 R20, they likely engage PP1γ via distinct mechanisms.

The PP1 active site is fully accessible to substrates in the RRP1B:PP1 complex

To understand how the RRP1B PP1-binding domain binds PP1, we determined the crystal structure of the $RRP1B_{682–727}$: $PP1\alpha_{7–300}$ Q20R holoenzyme (Figures 3D and 3E; Table S2) (1.8 Å resolution, hereafter referred to as RRP1B:PP1 complex; complexes with longer constructs of RRP1B crystallized but resulted in low-resolution, anisotropic data). Two complexes were present in the asymmetric unit and, for both complexes, strong, interpretable electron density was observed for all residues in PP1 and residues 682–727 of RRP1B. As expected, RRP1B ^{683}KVTF^{686} binds PP1 via the PP1 RVxF binding pocket.[15] However, as anticipated on the basis of the NMR data, RRP1B residues beyond the RVxF motif also bind directly to PP1 in a manner not observed for any other PP1 regulator (Figures 3D and 3E). The interaction with PP1 involves all 45 amino acids of the RRP1B binding domain, extending from the RVxF binding pocket, toward the C terminus, down the back of PP1 and ending at the SILK binding pocket (Figure 4A). Consistent with the tight affinity between RRP1B and PP1, complex formation buries a total of ~4,500 $Å^2$ of solvent-accessible surface area (4,440 $Å^2$, complex 1; 4,575 $Å^2$, complex 2), one of the largest buried surface area values observed for any PP1 holoenzyme (Figure 4B). Because RRP1B binds only the top and back of PP1, the PP1 active site, as well as the C-terminal, the acidic, and the hydrophobic substrate binding grooves, is fully accessible for dephosphorylating RRP1B:PP1-specific substrates.

RRP1B binds PP1, in part, via RVxF and ΦΦF[xF] SLiMs

The RRP1B residues that become most buried upon complex formation define five key interaction sites in the RRP1B:PP1 complex (Figure 4B). The first sites are bound by the RVxF and ΦΦ SLiMs, with the RVxF SLiM being the most highly conserved SLiM in the RRP1B:PP1 binding domain (determined using the iterative profile-HMM search program JACKHMMER for identifying remote homologs, 319 distinct sequences; Figure 4C). RRP1B residues ^{683}KVTFGL^{688} bind the extended RVxF binding pocket, with the “L” residue defining the RVxF hydrophobic “lid” (Figure 4D).[10] Residues ^{693}TA^{694} bind the ΦΦ pocket, forming a short β strand that hydrogen bonds with PP1 β14, while $RRP1B_{Phe696}$ binds a hydrophobic pocket defined by PP1 residues $PP1_{Pro270}$, $PP1_{Leu296}$, and $PP1_{Pro298}$ (Figure 4E). This is the fifth regulator shown to bind this pocket using a Phe residue, establishing it as a bona fide SLiM interaction site on PP1 (Figure 4F). Thus, the ΦΦ SLiM is most accurately defined as either ΦΦ or ΦΦ[xF], where the square brackets indicate that the “xF” residues are present in that subset of regulators. Together, this structure firmly establishes that the majority of PP1-specific regulators bind PP1, in part, using a general RVxF and ΦΦ[xF] SLiMs (Figure 4F; RVxF/ΦΦ: NIPP1, KNL1; RVxF/ΦΦ[xF]: RRP1B, PNUTS, RepoMan, Ki-67, Phactr1, R15B/GADD34, spinophilin/neurabin, G_M/G_L).[8,10,11,29–35]

PP1γ isoform specificity residue arginine 20 stabilizes a pocket used exclusively by PP1β/PP1γ-specific regulators, the β/γ-specificity pocket

While the RRP1B:PP1 complex established that RRP1B binds PP1 via a general RVxF-ΦΦ[xF] SLiM, the remaining interactions lead to a conformation unique to the RRP1B:PP1 holoenzyme. First, RRP1B forms a sharp kink that directs the chain to the back side of PP1 (i.e., opposite the PP1 active site). Beyond the kink, RRP1B interacts extensively with PP1 via conserved and atypical mechanisms at three key sites (Figures 4G–4I; except for one loop—RRP1B ^{706}SPTGPSR^{712}, Figure 4J—all interactions between RRP1B and PP1 are identical between both RRP1B:PP1 complexes present in RRP1B:PP1 crystals).

RRP1B residues ^{702}SILV^{705}, especially RRP1B$_{Ser702}$, bind a deep, mostly hydrophobic pocket between the PP1 N-terminal loop and the core catalytic domain (Figure 5A, left). The N-terminal loop of PP1 includes residue 20 (β/γ, Arg; α, Gln), a residue we showed determines the isoform specificity of RRP1B (Figure 2). These data suggest that the interaction at this site is responsible for the isoform selectivity of RRP1B for PP1β/PP1γ. Unusually, PP1$_{Arg20}$ does not make direct contact with RRP1B as might be expected. Instead, the side chain of PP1$_{Glu77}$, which in free PP1 blocks the N-terminal loop hydrophobic pocket, rotates to form a bidentate salt bridge with PP1$_{Arg20}$, exposing the pocket for regulator binding (Figure 5A, right). Regulator binding is further stabilized by a rotation of the PP1$_{Arg74}$ side chain, which stabilizes the sharp turn of the RRP1B chain via multiple hydrogen bonds (Figure 5A, right). Identical interactions are observed in both the Ki-67:PP1 and RepoMan:PP1 complexes, the only other regulators whose specificities for PP1β/PP1γ also depend on the identity of PP1 residue 20. Together, these data show that this PP1$_{Arg20}$ stabilized interaction site is used exclusively by regulators that are specific for PP1β and PP1γ, and thus we have renamed this PP1 pocket the β/γ-specificity pocket.

Discovery of an atypical regulator interaction pocket on PP1, the AF-binding pocket

The next major interaction between RRP1B and PP1 is mediated by RRP1B residues ^{712}RVAF^{715}. These residues, especially ^{714}AF^{715}, bind a hydrophobic pocket defined largely by PP1 helix α1 (Figure 5B, left). This interaction is stabilized, in part, by multiple salt bridges between RRP1B$_{Arg712}$ and PP1$_{Glu84}$ and PP1$_{Glu77}$ and a hydrogen bond between the RRP1B$_{Arg712}$ carbonyl and PP1$_{Arg20}$ (Figure 5B, right; the latter interaction explains, in part, why the increased relative affinity of RRP1B for PP1γ versus PP1α is 22-fold compared with that observed for RepoMan, 4-fold, which makes no direct interactions with Arg20$_{PP1}$). Like RRP1B$_{Ser702}$, both RRP1B$_{Ala714}$ and RRP1B$_{Phe715}$ become almost fully buried upon complex formation, suggesting that they contribute significantly to binding (Figure 4B). Consistent with this, they are also highly conserved among RRP1B sequences (Figure 4C). To quantify the contribution of RRP1B$_{Phe715}$ for PP1 binding, we measured the affinity ofWTRRP1B and the RRP1B$_{F715A}$ variant for PP1 using surface plasmon resonance (SPR). WT RRP1B$_{682–727}$ binds PP1 (PP1α$_{7–330}$ Q20R) with a K_D of 22.5 nM (essentially identical to that determined using ITC; Figure 5C and Table S1). The single point mutation RRP1B$_{F715A}$ (AF → AA) weakens PP1 binding by 7-fold (K_D = 157 ± 12 nM; Figure 5D and Table S3), confirming the importance of this interaction for RRP1B binding.

RRP1B contains a non-canonical SILK motif

The last major interaction between RRP1B and PP1 is between RRP1B residues ^{724}GVLK^{727} and the PP1 SILK motif binding pocket.[36] Although only G/SILK motifs have thus far been observed to bind the PP1 SILK binding pocket,[31,36] our structure shows that GVLK sequences also bind effectively, with RRP1B$_{Val725}$ binding the deep hydrophobic pocket typically occupied by the “Ile” residues of SILK SLiMs (Figure 4I). Thus, the RRP1B:PP1 complex expands the experimental definition of the SILK SLiM to G/S-I/V-L/V-K. To test the contribution of the SILK motif for PP1 binding, we again used SPR. Deleting the SILK motif (RRP1B$_{\Delta SILK}$: RRP1B$_{682–723}$) weakens PP1 binding 5-fold, to 114 ± 7 nM (Figure 5E and Table S3). This is a modest reduction in affinity compared with the same deletion in other SILK-containing regulators[7] and is consistent with the observation that the RRP1B$_{Val725}$ side chain does insert as deeply into the SILK binding pocket as isoleucine side chains (this work) and that mutating the I2 SILK isoleucine to glycine, alanine, phenylalanine, or tryptophan reduces I2-mediated inhibition of PP1 up to >250-fold.[37] Because of the extensive interactions of RRP1B beyond its RVxF motif, we reasoned that RRP1B may bind PP1 in the absence of a functional RVxF motif, a motif that for most regulators is strictly required for PP1 binding. To test this, we generated the RRP1B$_{V684A/F686A}$- double mutant (RRP1B$_{RAxA}$; RVxF → RAxA). While PP1 binding by RRP1B$_{RAxA}$ is severely impacted (435-fold reduction in affinity, K_D = 9,800 nM), binding is not abolished, reflecting the importance of the interactions beyond the RRP1B RVxF motif for PP1 binding (Figure 5F and Table S3).

Regulating RRP1B:PP1 complex formation by phosphorylation

PP1 holoenzyme assembly is often inhibited by regulator phosphorylation. In particular, a comprehensive study established that phosphorylation of the “x” residue in regulator RVxF motifs (RV-S/T-F), including that of RRP1B, potently inhibits regulator binding.[38] However, the emerging view is that the phosphorylation of residues outside the RVxF can also regulate the assembly of PP1 holoenzymes.[11,31,39] Of the six S/T residues in RRP1B outside the RVxF motif, three (RRP1B$_{T693}$, RRP1B$_{Ser702}$, and RRP1B$_{S706}$) have been identified in multiple high-throughput proteomic studies, with two having high probabilities for phosphorylation by protein kinase A (RRP1B$_{Ser702}$) or CDK5 (RRP1B$_{S706}$) (Table S4).[40,41] Only one of these residues, RRP1B$_{Ser702}$, makes extensive interactions with PP1, with the Ser702 side chain binding the outer edge of the β/γ-specificity pocket (the latter interaction is atypical for an IDP-folded protein interaction, as key anchoring interactions are often mediated by large hydrophobic residues, i.e., the “V” and “F” residues of RVxF motifs). Thus, we reasoned that RRP1B binding may be regulated by phosphorylation of S702. To test this, we first modeled RRP1B$_{Ser702}$ as an Asp (phosphomimetic, RRP1B$_{S702D}$) or phosphorylated serine (RRP1B$_{pSer702}$) into the RRP1B:PP1 structure. The model showed that an Asp and pSer side chain would sterically clash with PP1 (Figures 6A–6C), suggesting it would disrupt binding. We then measured the affinity of RRP1B$_{S702D}$ for PP1 using SPR. As predicted by the modeling, the affinity of RRP1B$_{S702D}$ for PP1 weakened significantly compared with WT (15-fold; K_D = 329 ± 16 nM, Figure 6D and Table S3).

We then used fluorescent cell imaging and pull-down assays to quantify the impact of S702 phosphorylation on PP1γ binding in cells. We generated the S702D mutant in the

pEGFP(C1)-RRP1B plasmid (pEGFP(C1)-RRP1B$_{S702D}$) and used a fluorescent two-hybrid assay to monitor PP1γ and either RRP1B, RRP1B$_{RAxA}$, or RRP1B$_{S702D}$ co-localization in cells. Specifically, HeLa/TetU2 cells with 256 Lac operator repeats stably integrated into the genome (256xLacO repeats) were transiently transfected to co-express mCherry-LacRepressor-NLS-PP1γ plus either GFP alone, GFP-RRP1B (WT), GFP-RRP1B$_{RAxA}$, or GFP-RRP1B$_{S702D}$. Live cell imaging showed that while RRP1B binds the LacR-PP1γ tethered to the LacO repeats (Figure 6E), resulting in its accumulation at the gene locus, no accumulation of GFP (Figure 6E), RRP1B$_{RAxA}$ (Figure 6G), or RRP1B$_{S702D}$ (Figure 6H) is observed in the majority of cells. These data demonstrate that the weakened affinity of RRP1B$_{S702D}$ for PP1 essentially abolishes its ability to bind PP1γ *in vivo*. GFP-trap pull-down assays are consistent with this result (Figure 6H). Namely, while GFP-RRP1B transiently expressed in U2OS cells readily binds and pulls down endogenous PP1γ, essentially no PP1γ is pulled down by either GFP-RRP1B$_{RAxA}$ or GFP-RRP1B$_{S702D}$ (2.1% ± 0.6% and 4.6% ± 2.0%, respectively, compared with WT; Figure 6J), even though both show the same nucleolar localization as the WT protein (Figure S3). Together, these data show that phosphorylation of RRP1B$_{Ser702}$ inhibits RRP1B:PP1 holoenzyme assembly and further demonstrates that PP1 holoenzyme formation can be regulated by the phosphorylation of residues outside the canonical RVxF motif.

DISCUSSION

The cellular localization and substrate specificity of PP1 is determined by its interaction with more than 200 regulatory proteins to form functional PP1 holoenzymes.[3,4] While biochemical studies established that most regulators bind PP1 via an RVxF SLiM, structural studies over the last years revealed that most regulators bind PP1 via extended interaction domains and distinct mechanisms.[2] This structural variation is possible because most regulators are IDPs typically containing multiple distinct SLiM sequences that bind the corresponding PP1 SLiM binding grooves in a modular manner.[42,43] However, while the RVxF SLiM was identified in PP1 regulators using biochemical studies, the remainder of PP1-specific SLiMs, and their corresponding interaction site(s) on PP1, have only been able to be identified using experimental structural studies.[10,11,30,36] This is because SLiMs are short (~4–6 amino acids) and often not strictly conserved, making their presence in a regulator, and their corresponding binding site on PP1, nearly impossible to predict.[44,45] Our structure of the RRP1B:PP1 holoenzyme complex reveals that RRP1B binds PP1 via sequences that extend far beyond the canonical RVxF SLiM; however, it does so via interactions that, together, are atypical compared with any previously molecularly studied regulator. These interactions have not only expanded the definitions of the known PP1-specific RVxF and SILK motifs but have also led to the discovery of two additional SLiM interaction sites on PP1 that are likely used by other regulators for PP1 binding.

First, our structure confirms that the ΦΦ SLiM is often extended by two amino acids to ΦΦ[xF], with a Phe residue binding a hydrophobic pocket near the C terminus. This is because when comparing the regulator:PP1 holoenzymes that have been determined to date (17 of the estimated 200), 90% bind PP1 using both the RVxF SLiM and an ΦΦ[xF] sequences. Because of the sequence variability in the ΦΦ sequence and the differences in the number of residues between the RVxF and ΦΦ sites, identifying these motifs in regulators

using sequence alone is nearly impossible.[42] The RRP1B:PP1 holoenzyme structure also showed that RRP1B binds PP1 using a non-canonical SILK motif (^{724}GVLK^{727}; the SILK motif is the most prevalent SLiM after the RVxF and ΦΦ motifs) that binds the PP1 SILK binding pocket. This expands the experimentally confirmed definition of the SILK motif (G/S-V/I-L-K)[31,36] and highlights the likelihood that other PP1 regulators with less conventional SILK sequences also use the SILK site for PP1 binding.

Furthermore, the structure revealed the presence of an interaction site on PP1 not previously used by any other regulator whose holoenzyme structure is known, the AF-binding pocket. It also established how PP1γ isoform selectivity is achieved via an interaction at a PP1 pocket we now term the β/γ-specificity pocket. Although the role of PP1 residue 20 was previously identified to play a role in PP1γ selectivity by its PP1γ-specific regulators,[26] how Arg20 mediated this selectivity was not fully understood until structural studies,[11] including this work. Both interactions expand the repertoire of PP1 SLiM binding sites available for regulator binding. The hydrophobic AF-binding pocket is located between the PP1 N terminus and the PP1 catalytic domain, engaging RRP1B residues ^{714}AF^{715}. Notably, these residues are part of a potential second RVxF motif (^{712}RVAF^{715}), giving rise to the possibility that RVxF motifs identified in other PP1 regulators might bind to this site and not the canonical RVxF binding pocket. As the short AF sequence does not yet allow for the description of a general binding motif (other than a second general ΦΦ-type motif), future studies of other PP1 regulators will be necessary to fully define the SLiM for this binding groove.

Finally, our work also demonstrates how PP1$_{Arg20}$ (β/γ) both reveals and stabilizes the hydrophobic β/γ-specificity pocket on PP1. Namely, PP1$_{Glu77}$, which normally blocks access to this pocket, rotates to form a bidentate salt bridge with PP1$_{Arg20}$, an interaction not possible with PP1$_{Gln20}$ (α; Figure 5A). This rigidifies the PP1$_{Glu77}$ conformation and, in turn, renders the hydrophobic pocket fully accessible to regulators. IDP regulators that are PP1β/PP1γ specific, such as RRP1B, require this pocket for binding, which explains why mutating a single amino acid in PP1α, Q20R, renders it “PP1γ-like,” allowing it to bind PP1β/PP1γ-specific regulators. This mechanism is distinct from that described for iASPP/ASPP1/ASPP2,[12,25] in which a folded SH2 domain immediately adjacent to the RVxF motif binds specifically to the PP1 C terminus and achieves isoform selectivity by distinguishing the largely divergent C-terminal PP1 sequences. Together, these data suggest that while PP1 isoform selectivity is achieved via one of two mechanisms—either through the interaction of a regulator folded domain with the PP1 C terminus (ASPP/PP1) or via binding of an IDP regulator via the PP1 β/γ-specificity pocket (RRP1B/PP1)—when the regulator is intrinsically disordered throughout its sequence, especially around the RVxF motif, it likely achieves specificity for PP1β/PP1γ by binding directly to the β/γ-specificity pocket.

In support of this model, the PP1 regulators Ki-67 and RepoMan also bind directly to the β/γ-specificity pocket.[11] Like RRP1B, Ki-67 and RepoMan (RM) were predicted to be nearly exclusively disordered and shown to selectively recruit PP1β/PP1γ, a recruitment later demonstrated to require PP1 Arg20.[11] A comparison of the Ki-67:PP1 and RM:PP1 structures with that of RRP1B:PP1 shows that all three regulators bind the β/γ-specificity

pocket and do so via identical structural mechanisms (Figure 7A), despite having largely divergent sequences (Figure 7B). In particular, the bound conformations of the RVxF, ΦΦ[xF], and β/γ-specificity pocket binding residues that Ki-67, RepoMan, and RRP1B adopt are highly similar, with the loops connecting the ΦΦ[xF] motif Phe to the β/γ-specificity pocket binding residue, adopting identical conformations owing to conserved hydrogen bonds between the regulator carbonyls and $PP1_{Arg74}$ (Figures 7C–7F). In contrast, the structures of their C-terminal PP1 interacting domains are highly divergent, with Ki-67 and RepoMan extending back toward the RVxF binding pocket and RRP1B extending in the opposite direction toward the SILK binding pocket (Figure 7A).

Together, these results suggest that β/γ-specific IDP regulators bind PP1 similarly, namely, using an RVxF and ΦΦ[xF] motif followed immediately by the β/γ-specificity pocket binding residues; while the latter is not conserved in sequence, the near-identical conformations of this loop demonstrate that it is constrained by length. PP1 is responsible for 80% of the Ser/Thr dephosphorylation in the nucleolus, due largely to the RRP1B and Ki-67 targeting of these isoforms to the nucleolus.[15] However, there are additional nucleolar PP1 regulators (Figure 7G). In particular, we previously identified MPP10, the U3 small nucleolar RNA-associated protein that binds the 90S pre-ribosome to be highly enriched in the nucleolus and bind specifically to PP1γ.[15] Our data predict that, like RRP1B, MPP10 also likely binds the β/γ-specificity pocket to achieve PP1β/PP1γ isoform selectivity. Confirming this will require experimental validation, as will determining whether residues beyond this motif also contribute to PP1 binding, owing to the highly divergent nature of the sequences that engage this pocket (Figure 7B).

Finally, we also show that a phosphomimetic mutation in RRP1B outside of the RRP1B RVxF motif, S702D, not only reduces its affinity for PP1 15-fold *in vitro* but also abolishes its ability to recruit PP1γ in cells (Figure 6), nearly to the same extent as mutating that canonical RVxF motif to RAxA. These data support the emerging view that PP1 holoenzyme assembly is not only regulated by the phosphorylation status of the “x” residue in the RVxF motif but also via the phosphorylation of residues outside this motif that interact directly with PP1 (Figure 7H). Together, our data underscore the critical need for integrated molecular biophysical and structural studies to comprehensively define the mode(s) of interaction for all PP1 holoenzymes. These studies will fully define the PP1 regulatory binding code through the discovery of all interaction sites that still need to be identified.

Limitations of the study

Our detailed structural and functional analysis of the RRP1B:PP1 holoenzyme defines the complex molecular protein-protein interactions necessary to achieve PP1 isoform specificity and holoenzyme function in the nucleolus. A potential limitation of the study is that while the bioinformatic, structural, biophysical, and cellular data show that S702 phosphorylation inhibits RRP1B:PP1 holoenzyme assembly, the kinase that phosphorylates S702 is not yet known, and our studies were limited to analysis of the effects of a phosphomimetic mutation (S702D). Thus, the signaling events that result in phosphorylation at this site, and its functional relevance, remain to be defined. For all the cell-based assays, exogenous tagged

RRP1B and PP1 constructs were overexpressed against a background of their endogenous counterparts. Introducing mutations directly into the endogenous proteins, e.g., by CRISPR-Cas9-based genome editing, would provide additional information about the impact of the disruption of specific contact points on both the stability and the physiological function of the holoenzyme complex.

STAR★METHODS

RESOURCE AVAILABILITY

Lead contact—Further information and requests for resources and reagents should be directed to and will be fulfilled by the lead contact Rebecca Page (rpage@uchc.edu).

Materials availability—Plasmids and all unique reagents generated in this study are available from the lead contact with a completed Materials Transfer agreement.

Data and code availability

- All NMR chemical shifts have been deposited in the BioMagResBank (BMRB 51132). Atomic coordinates and structure factors have been deposited in the Protein DataBank (PDB: 7T0Y).
- This paper does not report original code.
- Any additional information required to reanalyze the data reported in this paper is available from the lead contact (rpage@uchc.edu) upon request.

EXPERIMENTAL MODEL AND SUBJECT DETAILS

Cells—All cell work was carried out in human osteosarcoma epithelial cells (U2OS).

METHOD DETAILS

Protein expression—The coding sequence of human $RRP1B_{657–758}$ containing an N-terminal his_6-tag followed by a TEV (tobacco etch virus) protease cleavage site was synthesized by DNA 2.0. The coding sequences of human $RRP1B_{657–758}$, $RRP1B_{677–736}$ and $RRP1B_{682–727}$ were subcloned into a pET-M30-MBP vector containing an N-terminal his_6-tag followed by maltose binding protein (MBP) and a TEV (tobacco etch virus) protease cleavage site. *Escherichia coli* BL21 (DE3) cells (Agilent) were transformed with RRP1B expression vectors. Freshly transformed cells were grown at 37°C in LB broth containing kanamycin antibiotics (50 μg/ml) until they reached an optical density (OD_{600}) of 0.6–0.8. Protein expression was induced by addition of 1 mM β-D-thiogalactopyranoside (IPTG) to the culture medium, and cultures were allowed to grow overnight (18–20 hours) at 18°C. Cells were harvested by centrifugation (6000 × g, 15 min, 4°C) and stored at −80°C until purification. Expression of uniformly ^{13}C- and/or ^{15}N-labeled protein was carried out by growing freshly transformed cells in M9 minimal media containing 4 g/L [^{13}C]-D-glucose and/or 1 g/L $^{15}NH_4Cl$ (Cambridge Isotopes Laboratories) as the sole carbon and nitrogen sources, respectively. $RRP1B_{682–727}$ variants ($RRP1B_{S702D}$: $RRP1B_{682–727}$ S702D, $RRP1B_{F715A}$: $RRP1B_{682–727}$ F715A, $RRP1B_{RAxA}$: $RRP1B_{682–727}$ V684A/F686A, $RRP1B_{\Delta SILK}$: $RRP1B_{682–723}$) were generated by site-directed mutagenesis,

sequence verified, and purified as described below. N-terminal cloning artifact GAMGYT was removed from $RRP1B_{682–727}$ using GeneArt Gibson assembly according to the manufacturer protocol (Invitrogen) to generate the $RRP1B_{682–727}$ construct that formed crystals that diffract to high resolution (see crystallization). Cloning and expression of $PP1\alpha_{7–300}$, $PP1\alpha_{7–300}$ Q20R, $PP1\alpha_{7–330}$ Q20R, $PP1\gamma_{7–308}$ and $PP1\gamma_{7–323}$ was performed as follows (see also[10,11,51,52]). Briefly, PP1 constructs were co-transformed with the pGRO7 plasmid encoding the chaperone GroEL/GroES (Takara) into BL21 (DE3) cells (Agilent). The cells were grown in LB medium supplemented with 1 mM $MnCl_2$ at 30°C to an OD_{600} of ~ 0.5, then arabinose was added (2 g/L) to induce the expression of the GroEL/GroES chaperone. When OD_{600} was ~ 1, the temperature was lowered to 10°C (ice-bath) and the expression of PP1 was induced with 0.1 mM IPTG for ~ 20 h. The cells were harvested by centrifugation, suspended in fresh LB medium (again supplemented with 1 mM $MnCl_2$ and 200 μg/ml of Cam to eliminate all ribosome activity) and agitated for 2 h at 10°C. Harvested cells were frozen and stored at − 80°C.

Protein purification.: *E. coli* BL21(DE3) cell pellets expressing RRP1B ($RRP1B_{657–758}$, $RRP1B_{677–736}$, $RRP1B_{682–727}$, $RRP1B_{S702D}$, $RRP1B_{F715A}$, $RRP1B_{RAxA}$ and $RRP1B_{\Delta SILK}$) were resuspended in ice-cold lysis buffer (50 mM Tris pH 8.0, 500 mM NaCl, 5 mM imidazole, 0.1% Triton X-100 and an EDTA-free protease inhibitor tablet [Roche]) and lysed by high pressure homogenization (Avestin EmulsiFlex C3). Lysate was clarified by centrifugation (45,000 ×*g*, 45 min, 4°C) and the supernatant was loaded under gravity onto a Ni^{2+}-NTA beads (GE Healthcare) pre-equilibrated with 50 mM Tris pH 8.0, 500 mM NaCl and 5 mM imidazole. Protein was eluted with 4 column volumes (20 ml) with 50 mM Tris pH 8.0, 500 mM NaCl and 500 mM imidazole. Fractions with RRP1B were pooled and dialyzed with tobacco etch virus (TEV) protease overnight at 4°C against 50 mM Tris pH 8.0, 500 mM NaCl, 0.5 mM TCEP to cleave the MBP-His_6-tag. The cleaved protein was incubated with the Ni^{2+}-NTA beads (GE Healthcare) to remove the TEV protease and cleaved MBP-His_6-tag. The flow-through was collected, heat purified at 95°C (15 min), concentrated and further purified using size-exclusion chromatography (SEC; Superdex 75 26/60 [GE Healthcare]) equilibrated in either NMR Buffer (20 mM Bis-Tris pH 6.8, 150 mM NaCl, 0.5 mM TCEP) or SEC/SPR/ITC buffer (20 mM Tris pH 8.0, 500 mM NaCl, 0.5 mM TCEP, 1 mM $MnCl_2$). Fractions were pooled, concentrated and stored at −20°C.

PP1 was purified as described previously.[10] In brief, PP1 ($PP1\alpha_{7–300}$, $PP1\alpha_{7–300}$ Q20R, $PP1\alpha_{7–330}$ Q20R, $PP1\gamma_{7–308}$ and $PP1\gamma_{7–323}$) was lysed in PP1 Lysis Buffer (25 mM Tris pH 8.0, 700 mM NaCl, 5 mM imidazole, 1 mM $MnCl_2$, 0.01% Triton X-100), clarified by centrifugation (45,000 ×*g*, 45 min, 4°C) and immobilized on Ni^{2+}-NTA resin. Bound His_6-PP1 was washed with PP1 Buffer A (25 mM Tris pH 8.0, 700 mM NaCl, 5 mM imidazole, 1 mM $MnCl_2$), followed with a stringent wash containing 6% PP1 Buffer B (25 mM Tris pH 8.0, 700 mM NaCl, 250 mM imidazole, 1 mM $MnCl_2$) at 4°C. The protein was eluted using PP1 Buffer B and His_6-tagged PP1 was purified using SEC (Superdex 200 26/60 [GE Healthcare]) pre-equilibrated in SEC Buffer (20 mM Tris pH 8, 500 mM NaCl, 0.5 mM TCEP, 1 mM $MnCl_2$). Peak fractions were incubated overnight with TEV protease at 4°C. The cleaved protein was incubated with Ni^{2+}-NTA beads (GE Healthcare),

PP1 without His_6 in the flow-through was collected and immediately used for our study. All experiment were performed with freshly purified PP1.

RRP1B$_{657–758}$:PP1$\gamma_{7–308}$ (for NMR studies) and RRP1B$_{682–727}$:PP1$\alpha_{7–300}$ Q20R complex formation (for crystallography studies).: To purify the RRP1B$_{657–758}$:PP1$\gamma_{7–308}$ complex for NMR spectroscopy, purified PP1$_{7–308}$ without His6 from above step was combined with excess ^{15}N- labeled RRP1B$_{657–758}$, concentrated and purified using SEC (pre-equilibrated in NMR buffer). Fractions containing the holoenzyme complex was concentrated to 0.1 mM for NMR studies. To generate the RRP1B$_{682–727}$:PP1$\alpha_{7–300}$ Q20R complex for crystallization, purified PP1 without His6 was incubated with 1.5x excess of purified RRP1B$_{682–727}$ and the complex was purified using SEC in crystallization buffer (20 mM Tris pH 8.0, 500 mM NaCl, 0.5 mM TCEP, 1 mM $MnCl_2$). Final complex concentration was ~3 mg/mL for crystallization trials using vapor diffusion (sitting drop).

NMR spectroscopy—NMR experiments were acquired on a Bruker AvanceIIIHD 850 MHz spectrometer, both equipped with a TCI HCN-z cryoprobe at 298 K. NMR spectra for the assignment of RRP1B$_{657–758}$ were acquired using ^{15}N,^{13}C-labeled protein at a final concentration of 0.8 mM in 20 mM Bis-Tris pH 6.8, 150 mM NaCl, 0.5 mM TCEP and 90% H_2O/10% D_2O. The following spectra were used to complete the sequence specific backbone assignment: 2D [^{1}H,^{15}N] HSQC, 2D [^{1}H,^{13}C] HSQC, 3D HNCA, 3D HN(CO)CA, 3D CBCA(CO)NH, 3D (H)CC(CO)NH and 3D HNCACB. All spectra were processed using Topspin 2.1/3.0/3.1 (Bruker, Billerica, MA), and chemical shift assignments were achieved using Cara (http://cara.nmr.ch).

For RRP1B$_{657–758}$ all residues but Arg 658, Asn689, Lys698, Thr699, Asp700 and two cloning artifacts (His2 and Met3) are assigned. The interaction between RRP1B$_{657–758}$ with PP1$\gamma_{7–308}$ was studied by direct comparison of the 2D [^{1}H,^{15}N] HSQC spectra of free ^{15}N-labeled RRP1B$_{657–758}$ and in complex with PP1$\gamma_{7–308}$. The final concentration was 0.1 mM RRP1B$_{657–758}$ in complex with PP1$\gamma_{7–308}$ in NMR buffer and 90% H_2O/10% D_2O. The spectra were processed using Topspin 3.1 and analyzed using NMRFAM-Sparky.[46]

Crystallization and structure determination of the RRP1B$_{682–727}$:PP1$\alpha_{7–300}$ Q20R complex—Initial crystals of the RRP1B$_{682–727}$:PP1$\alpha_{7–300}$ Q20R holoenzyme complex resulted in low resolution anisotropic data (AMX, NSLSII) with hierarchical cluster analysis of datasets collected from multiple crystals producing a dataset suitable for phasing using molecular replacement using PP1 as a search model (4MOV; a manuscript describing the heirarchical cluster analysis is in preparation). While density for RRP1B was clearly visible, RRP1B could not be accurately modeled. However, it was observed that N-termini of two RRP1B molecules were clashing at a 2-fold axis. Deletion of the RRP1B N-terminal cloning artifact GAMGYT resulted in a new crystal form of the RRP1B$_{682–727}$:PP1$\alpha_{7–300}$ Q20R complex (0.1 M Na-HEPES, 0.1 M MOPS acid pH 7.5, 20% (v/v) ethylene glycol; 10% PEG8000 and halogens [0.09 M Sodium fluoride; 0.09 M Sodium bromide and 0.09 M Sodium iodide], condition 1–14 of the Morpheus Screen, Molecular Dimensions). Crystals were cryo-protected in 100% ethylene glycol overnight and then flash frozen in liquid N_2. Diffraction data was collected at Beamline ID23B, GM/CA@APS and processed using gmcaproc pipeline.[53] The structure

of $RRP1B_{682–727}$:$PP1\alpha_{7–300}$ Q20R was determined by molecular replacement using Phaser as implemented in PHENIX.[47] PP1 (4MOV) was used as the search model.[10] A solution was obtained in space group $P2_12_12$. The model was completed using iterative rounds of refinement in PHENIX and manual building using Coot.[48]

Isothermal titration calorimetry (ITC)—His_6-tagged PP1 ($PP1\gamma_{7–308}$, $PP1\gamma_{7–323}$, $PP1\alpha_{7–330}$ and $PP1\alpha_{7–330}$ Q20R) were purified as described for ITC analysis.[10,11] ITC experiments testing the interaction between $RRP1B_{657–758}$ and $RRP1B_{677–736}$ with His_6-tagged PP1γ ($PP1\gamma_{7–323}$ and $PP1\gamma_{7–308}$), and $RRP1B_{657–758}$ with His_6-tagged PP1α ($PP1\alpha_{7–330}$ and $PP1\alpha_{7–330}$ Q20R) were performed at 25°C using either VP-ITC (Malvern). Concentrations of PP1γ between 3 and 4 μM were used in the sample cell. RRP1B was titrated in 10 μL increments over 20 s at concentrations of 30 μM–40 μM (performed in duplicate). 25 injections were delivered during each experiment with a 250 s interval between titrations to allow for complete equilibration and baseline recovery, and the solution in the sample cell was stirred at 300 rpm to ensure rapid mixing. To determine the thermodynamic parameters (ΔH, ΔS, ΔG) and binding constant (K_a), data were analyzed with a one-site binding model assuming a binding stoichiometry of 1:1 using NITPIC,[49] SEDPHAT[50] and GUSSI.[50]

Surface plasmon resonance (SPR)—SPR measurements were performed using a 4-channel Reichert 4SPR instrument fitted with autosampler and a degassing pump (Reichert Technologies). SPR buffers containing 20 mM Tris pH 8.0, 500 mM NaCl, 1 mM $MnCl_2$, 0.5 mM TCEP, 0.05% Tween were prepared, sterile filtered, and degassed in autoclaved glassware prior to each experiment. Running buffer was used to prime and run both the sample and syringe pump reservoirs. Gold sensorchips modified with Ni-NTA-functionalized polycarboxylate (NiHC200M; XanTec bioanalytics GmbH) were installed and equilibrated under flow conditions (100 μL/min) for ≥60 min at 25°C. Surface contaminants were cleared from the chip surface by a pair of 120 μL injections of 2 M NaCl and 10 mM NaOH during the equilibration step. Experiments were conducted at 25°C with a 5 Hz sampling rate and were initiated by injecting 120 μL of His_6-PP1 ($^{Q20R}PP1\alpha_{7–330}$) constructs (40–80 nM) diluted in 20 mM Tris pH 8.0, 500 mM NaCl, 1 mM $MnCl_2$, 0.5 mM TCEP, 0.05% Tween onto channels 1 and 2 for 120 s at 50 μL/min which resulted in between 200 and 450 μRIU of surface loading (channel 3 and 4 were used as reference surfaces). The sensorchip was allowed to equilibrate for 5 min at 50 μL/min prior to beginning the experiments. The concentrations of $RRP1B_{682–727}$ and its variants ($RRP1B_{S702D}$, $RRP1B_{F715A}$, $RRP1B_{RAxA}$ and $RRP1B_{\Delta SILK}$) were measured using AccuOrange Protein Quantification Kit (Biotium). For measurements, $RRP1B_{682–727}$ and its variants ($RRP1B_{S702D}$, $RRP1B_{F715A}$, $RRP1B_{RAxA}$ and $RRP1B_{\Delta SILK}$) were diluted into running buffer from concentrated stocks, and a series of injection at different concentration of RRP1B were applied. 60 μL sample of RRP1B were respectively injected for 60 s at 50 μL/min followed by a dissociation step of 120 s–180 s; except for the experiment of the pair of $^{Q20R}PP1\alpha_{7–330}$ and $RRP1B_{682–727}$, for which 120 μL sample of $RRP1B_{682–727}$ were injected for 120 s at 50 μL/min followed by a dissociation step of 600 s. For all experiments, buffer blank injections were included at an interval of two sample injections to achieve double referencing, if any. Technical replicates were obtained by utilizing two channels per

chip coupled with stripping of the sensorchip with 350 mM EDTA pH 8, reconditioning the surface with 10 mM NaOH to remove non-specifically bound PP1 aggregates, charging the surface with 40 mM $NiSO_4$, and reloading fresh PP1 onto the surface. All replicates were generated with freshly diluted PP1 and RRP1B. Kinetic parameters were determined by curve-fitting using TraceDrawer software (Ridgeview Instruments AB) fit with a one-to-one model. Statistical analyses of SPR data were completed using Microsoft excel.

Plasmids and antibodies—The pEGFP(C1)-PP1α and pEGFP(C1)-PP1γ plasmids were previously described[14] and are available through Addgene (plasmids #44224 and #44225). The C-terminal truncation mutant pEGFP(C1)-PP1γΔ299–323 was derived from the full-length construct by PCR-based insertion of a premature STOP codon. The C-terminal chimera pEGFP(C1)-PP1γ(1–298)PP1α(299–330) was derived by PCR-based insertion of a SalI restriction site into the full-length construct at the relevant site, followed by digestion and ligation of the PP1α C-terminal coding sequence. The pEGFP(C1)-RRP1B and pEGFP(C1)-$RRP1B_{RAxA}$ (V684A/F686A) plasmids were previously described.[15] PP1 and RRP1B point mutants were derived using Quickhange mutagenesis (Agilent Technologies) and sequence confirmed. Antibodies that recognize RRP1B, RepoMan and ASPP2 were obtained from Abcam, PP1g antibodies were from Santa Cruz and GFP-antibodies from proteintech®. HRP-conjugated secondary antibodies were from ThermoFisher.

Cell culture—U2OS cells were obtained from ATCC and grown in Dulbecco's modified Eagles' medium (DMEM; Wisent Bioproducts Inc.) supplemented with 10% fetal calf serum and 100 U/mL penicillin and streptomycin (Wisent Bioproducts Inc). For transient overexpression of GFP and GFP-tagged constructs, cells were transfected using 1 mg/mL polyethylenimine (PEI) transfection reagent. For Western blot and immunoprecipitation experiments, whole cell extracts were prepared by scraping cells into ice-cold RIPA buffer (50 mM Tris pH 7.5, 150 mM NaCl, 1% NP-40, 0.5% deoxycholate, protease inhibitors), sonicating and clearing by centrifuging at 21000g for 10 min at 4°C. Total protein concentrations were measured using the Pierce BCA Protein Assay Kit (ThermoFisher).

Fluorescence imaging—For live imaging, cells were cultured in 35 μm optically clear polymer-bottom μ-dishes (ibidi) and transiently transfected for 18 hrs using PEI. Growth medium was replaced with Phenol Red-free CO_2 independent medium (ThermoFisher) and DNA stained by incubating the cells for 20 min at 37°C in medium containing 0.25 μg/m Hoechst No. 33342 (Sigma-Aldrich). Images were acquired using a DeltaVision CORE widefield fluorescence system fitted with 40x NA 1.2 and 60× NA 1.4 PlanApochromat objectives (Olympus), CoolSNAP charge-coupled device (CCD) camera (Roper Scientific) and environmental chamber. The microscope was controlled and images processed by SoftWorX acquisition and deconvolution software (GE Healthcare). All images are single, deconvolved optical sections.

Immunoprecipitation and Western blot—GFP fusion proteins were captured from cell extracts by incubating equal amounts of total protein for each condition with GFP-Trap_A beads (Chromotek) at 4°C for 1 hour,[54] with equal amounts of total protein extract

for each condition incubated with GFP-Trap_A beads (Chromotek) at 4°C for 1 hour. Following 3 washes with RIPA buffer, bound proteins were eluted with 2% SDS, resolved by electrophoresis on a NuPAGE 4–12% BisTris gel (Thermo Fisher) and transferred to nitrocellulose for Western blot analysis.[54] Chemiluminescent signals were captured using a ChemiDoc MP Imaging System (BioRad) and band intensities quantified using Image Lab software (BioRad).

Fluorescence two-hybrid (F2H) screens—A plasmid expressing mCherry-LacR-NLS-PP1γ was co-transfected with plasmids expressing GFP-tagged RRP1B (wild type or mutant) in a HeLa cell line that contains an integrated lacO array.[55] Negative controls included co-expression of mCherry-LacRNLS-PP1γ with free GFP, and co-expression of GFP-tagged regulatory proteins with mCherry-LacR-NLS. DNA was stained with Hoechst 33342 and cells imaged live to monitor co-localization of mCherry and GFP signals. 120 cells were scored for the accumulation of GFP and/or GFP-RRP1B variants at the gene locus and the percentage reported. Graphs report plot line profiles for red and green fluorescence over 2 μm at the gene locus.

QUANTIFICATION AND STATISTICAL ANALYSIS

For all SPR experiments, kinetic parameters were determined by curve-fitting using TraceDrawer software (Ridgeview Instruments AB) fit with a one-to-one model. Statistical analyses (mean ± SEM; 4–6 replicates) of SPR data were completed using Microsoft excel. For ITC experiments, data were analyzed with a one-site binding model assuming a binding stoichiometry of 1:1 using NITPIC,[49] SEDPHAT[50] and GUSSI.[50] Statistical analyses (mean ± SEM; 2–4 replicates) of ITC data were completed using Microsoft excel. For fluorescent imaging, images were processes by SoftWorX acquisition and deconvolution software (GE Healthcare). All images are single, deconvolved optical sections. For fluorescent F2H screens, 120 cells were scored for the accumulation of GFP and/or GFP-RRP1B variants at the gene locus and the percentage reported. Graphs report plot line profiles for red and green fluorescence over 2 μm at the gene locus. For IP and Western Blots, Chemiluminescent signals were captured using a ChemiDoc MP Imaging System (BioRad) and band intensities quantified using Image Lab software (BioRad).

Supplementary Material

Refer to Web version on PubMed Central for supplementary material.

ACKNOWLEDGMENTS

The authors thank Mr. Haejun Cho for help with RRP1B expression and purification. Support for work performed at the CBMS beamline LIX (16ID) | AMX (17ID-1) | FMX (17ID-2) at NSLS-II is provided by National Institute of General Medical Sciences P30GM133893 and DOE-BER KP1607011. NSLS-II is supported by DOE, BES-FWP-PS001. Crystallographic data were also collected at GM/CA@APS, which has been funded by the National Cancer Institute (ACB-12002) and the National Institute of General Medical Sciences (AGM-12006, P30GM138396). The Eiger 16M detector at GM/CA-XSD was funded by NIH grant S10 OD012289. This research used resources of the Advanced Photon Source, a US Department of Energy (DOE) Office of Science User Facility operated for the DOE Office of Science by Argonne National Laboratory under contract no. DE-AC02-06CH11357. This work was also supported by grants R01NS091336 from the National Institute of Neurological Disorders and Stroke and R01GM144483 from the National Institute of General Medical Sciences to W.P., discovery grants 06674 and

5018217 from the Natural Sciences and Engineering Research Council to L.T.-M., and R01GM098482 from the National Institute of General Medical Sciences to R.P.

REFERENCES

1. Brautigan DL (2013). Protein Ser/Thr phosphatases–the ugly ducklings of cell signalling. FEBS J. 280, 324–345. 10.1111/j.1742-4658.2012.08609.x. [PubMed: 22519956]
2. Brautigan DL, and Shenolikar S (2018). Protein serine/threonine phosphatases: keys to unlocking regulators and substrates. Annu. Rev. Biochem. 87, 921–964. 10.1146/annurev-biochem-062917-012332. [PubMed: 29925267]
3. Hendrickx A, Beullens M, Ceulemans H, Den Abt T, Van Eynde A, Nicolaescu E, Lesage B, and Bollen M (2009). Docking motif-guided mapping of the interactome of protein phosphatase-1. Chem. Biol. 16, 365–371. 10.1016/j.chembiol.2009.02.012. [PubMed: 19389623]
4. Lyons SP, Jenkins NP, Nasa I, Choy MS, Adamo ME, Page R, Peti W, Moorhead GB, and Kettenbach AN (2018). A quantitative chemical proteomic strategy for profiling phosphoprotein phosphatases from yeast to humans. Mol. Cell. Proteomics 17, 2448–2461. 10.1074/mcp.RA118.000822. [PubMed: 30228194]
5. Hoermann B, Kokot T, Helm D, Heinzlmeir S, Chojnacki JE, Schubert T, Ludwig C, Berteotti A, Kurzawa N, Kuster B, et al. (2020). Dissecting the sequence determinants for dephosphorylation by the catalytic subunits of phosphatases PP1 and PP2A. Nat. Commun. 11, 3583. 10.1038/s41467-020-17334-x. [PubMed: 32681005]
6. Aitken A, and Cohen P (1982). Isolation and characterisation of active fragments of protein phosphatase inhibitor-1 from rabbit skeletal muscle. FEBS Lett. 147, 54–58. 10.1016/0014-5793(82)81010-7. [PubMed: 7140990]
7. Kwon YG, Huang HB, Desdouits F, Girault JA, Greengard P, and Nairn AC (1997). Characterization of the interaction between DARPP-32 and protein phosphatase 1 (PP-1): DARPP-32 peptides antagonize the interaction of PP-1 with binding proteins. Proc. Natl. Acad. Sci. USA 94, 3536–3541. 10.1073/pnas.94.8.3536. [PubMed: 9108011]
8. Ragusa MJ, Dancheck B, Critton DA, Nairn AC, Page R, and Peti W (2010). Spinophilin directs protein phosphatase 1 specificity by blocking substrate binding sites. Nat. Struct. Mol. Biol. 17, 459–464. 10.1038/nsmb.1786. [PubMed: 20305656]
9. Terrak M, Kerff F, Langsetmo K, Tao T, and Dominguez R (2004). Structural basis of protein phosphatase 1 regulation. Nature 429, 780–784. 10.1038/nature02582. [PubMed: 15164081]
10. Choy MS, Hieke M, Kumar GS, Lewis GR, Gonzalez-DeWhitt KR, Kessler RP, Stein BJ, Hessenberger M, Nairn AC, Peti W, and Page R (2014). Understanding the antagonism of retinoblastoma protein dephosphorylation by PNUTS provides insights into the PP1 regulatory code. Proc. Natl. Acad. Sci. USA 111, 4097–4102. 10.1073/pnas.1317395111. [PubMed: 24591642]
11. Kumar GS, Gokhan E, De Munter S, Bollen M, Vagnarelli P, Peti W, and Page R (2016). The Ki-67 and RepoMan mitotic phosphatases assemble via an identical, yet novel mechanism. Elife 5, e16539. 10.7554/eLife.16539. [PubMed: 27572260]
12. Bertran MT, Mouilleron S, Zhou Y, Bajaj R, Uliana F, Kumar GS, van Drogen A, Lee R, Banerjee JJ, Hauri S, et al. (2019). ASPP proteins discriminate between PP1 catalytic subunits through their SH3 domain and the PP1 C-tail. Nat. Commun. 10, 771. 10.1038/s41467-019-08686-0. [PubMed: 30770806]
13. Choy MS, Moon TM, Ravindran R, Bray JA, Robinson LC, Archuleta TL, Shi W, Peti W, Tatchell K, and Page R (2019). SDS22 selectively recognizes and traps metal-deficient inactive PP1. Proc. Natl. Acad. Sci. USA 116, 20472–20481. 10.1073/pnas.1908718116. [PubMed: 31548429]
14. Trinkle-Mulcahy L, Sleeman JE, and Lamond AI (2001). Dynamic targeting of protein phosphatase 1 within the nuclei of living mammalian cells. J. Cell Sci. 114, 4219–4228. [PubMed: 11739654]
15. Chamousset D, De Wever V, Moorhead GB, Chen Y, Boisvert F-M, Lamond AI, and Trinkle-Mulcahy L (2010). RRP1B targets PP1 to mammalian cell nucleoli and is associated with Pre-60S ribosomal subunits. Mol. Biol. Cell 21, 4212–4226. 10.1091/mbc.E10-04-0287. [PubMed: 20926688]

16. Boisvert F-M, van Koningsbruggen S, Navascués J, and Lamond AI (2007). The multifunctional nucleolus. Nat. Rev. Mol. Cell Biol. 8, 574–585. 10.1038/nrm2184. [PubMed: 17519961]

17. Lam YW, and Trinkle-Mulcahy L (2015). New insights into nucleolar structure and function. F1000prime Rep. 7, 48. 10.12703/P7-48. [PubMed: 26097721]

18. Hernandez-Verdun D (2011). Assembly and disassembly of the nucleolus during the cell cycle. Nucleus 2, 189–194. 10.4161/nucl.2.3.16246. [PubMed: 21818412]

19. Trinkle-Mulcahy L, Andrews PD, Wickramasinghe S, Sleeman J, Prescott A, Lam YW, Lyon C, Swedlow JR, and Lamond AI (2003). Time-lapse imaging reveals dynamic relocalization of PP1gamma throughout the mammalian cell cycle. Mol. Biol. Cell 14, 107–117. 10.1091/mbc.e02-07-0376. [PubMed: 12529430]

20. Horsey EW, Jakovljevic J, Miles TD, Harnpicharnchai P, and Woolford JL (2004). Role of the yeast Rrp1 protein in the dynamics of pre-ribosome maturation. RNA N. Y. N 10, 813–827. 10.1261/rna.5255804.

21. Crawford NPS, Yang H, Mattaini KR, and Hunter KW (2009). The metastasis efficiency modifier ribosomal RNA processing 1 homolog B (RRP1B) is a chromatin-associated factor. J. Biol. Chem. 284, 28660–28673. 10.1074/jbc.M109.023457. [PubMed: 19710015]

22. Lee M, Dworkin AM, Gildea D, Trivedi NS, Crawford NPS, and Moorhead GBNISC Comparative Sequencing Program; NISC Comparative Sequencing Program (2014). RRP1B is a metastasis modifier that regulates the expression of alternative mRNA isoforms through interactions with SRSF1. Oncogene 33, 1818–1827. 10.1038/onc.2013.133. [PubMed: 23604122]

23. Paik JC, Wang B, Liu K, Lue JK, and Lin W-C (2010). Regulation of E2F1-induced apoptosis by the nucleolar protein RRP1B. J. Biol. Chem. 285, 6348–6363. 10.1074/jbc.M109.072074. [PubMed: 20040599]

24. Su W-C, Hsu S-F, Lee Y-Y, Jeng K-S, and Lai MMC (2015). A nucleolar protein, ribosomal RNA processing 1 homolog B (RRP1B), enhances the recruitment of cellular mRNA in influenza virus transcription. J. Virol. 89, 11245–11255. 10.1128/JVI.01487-15. [PubMed: 26311876]

25. Zhou Y, Millott R, Kim HJ, Peng S, Edwards RA, Skene-Arnold T, Hammel M, Lees-Miller SP, Tainer JA, Holmes CFB, and Glover JNM (2019). Flexible tethering of ASPP proteins facilitates PP-1c catalysis. Structure 27, 1485–1496.e4. 10.1016/j.str.2019.07.012. [PubMed: 31402222]

26. Lesage B, Beullens M, Ceulemans H, Himpens B, and Bollen M (2005). Determinants of the nucleolar targeting of protein phosphatase-1. FEBS Lett. 579, 5626–5630. 10.1016/j.febslet.2005.09.033. [PubMed: 16213493]

27. Dosztányi Z, Csizmok V, Tompa P, and Simon I (2005). IUPred: web server for the prediction of intrinsically unstructured regions of proteins based on estimated energy content. Bioinformatics 21, 3433–3434. 10.1093/bioinformatics/bti541. [PubMed: 15955779]

28. Marsh JA, Singh VK, Jia Z, and Forman-Kay JD (2006). Sensitivity of secondary structure propensities to sequence differences between alpha- and gamma-synuclein: implications for fibrillation. Protein Sci. 15, 2795–2804. 10.1110/ps.062465306. [PubMed: 17088319]

29. Choy MS, Yusoff P, Lee IC, Newton JC, Goh CW, Page R, Shenolikar S, and Peti W (2015). Structural and functional analysis of the GADD34:PP1 eIF2α phosphatase. Cell Rep. 11, 1885–1891. 10.1016/j.celrep.2015.05.043. [PubMed: 26095357]

30. O'Connell N, Nichols SR, Heroes E, Beullens M, Bollen M, Peti W, and Page R (2012). The molecular basis for substrate specificity of the nuclear NIPP1:PP1 holoenzyme. Structure 20, 1746–1756. 10.1016/j.str.2012.08.003. [PubMed: 22940584]

31. Bajaj R, Bollen M, Peti W, and Page R (2018). KNL1 binding to PP1 and microtubules is Mutually exclusive. Structure 26, 1327–1336.e4. 10.1016/j.str.2018.06.013. [PubMed: 30100357]

32. Fedoryshchak RO, Přechová M, Butler AM, Lee R, O'Reilly N, Flynn HR, Snijders AP, Eder N, Ultanir S, Mouilleron S, and Treisman R (2020). Molecular basis for substrate specificity of the Phactr1/PP1 phosphatase holoenzyme. Elife 9, e61509. 10.7554/eLife.61509. [PubMed: 32975518]

33. Kumar GS, Choy MS, Koveal DM, Lorinsky MK, Lyons SP, Kettenbach AN, Page R, and Peti W (2018). Identification of the substrate recruitment mechanism of the muscle glycogen protein phosphatase 1 holoenzyme. Sci. Adv. 4, eaau6044. 10.1126/sciadv.aau6044. [PubMed: 30443599]

34. Chen R, Rato C, Yan Y, Crespillo-Casado A, Clarke HJ, Harding HP, Marciniak SJ, Read RJ, and Ron D (2015). G-actin provides substrate-specificity to eukaryotic initiation factor 2α holophosphatases. Elife 4, e04871. 10.7554/eLife.04871. [PubMed: 25774600]
35. Yu J, Deng T, and Xiang S (2018). Structural basis for protein phosphatase 1 recruitment by glycogen-targeting subunits. FEBS J. 285, 4646–4659. 10.1111/febs.14699. [PubMed: 30422398]
36. Hurley TD, Yang J, Zhang L, Goodwin KD, Zou Q, Cortese M, Dunker AK, and DePaoli-Roach AA (2007). Structural basis for regulation of protein phosphatase 1 by inhibitor-2. J. Biol. Chem. 282, 28874–28883. 10.1074/jbc.M703472200. [PubMed: 17636256]
37. Huang HB, Horiuchi A, Watanabe T, Shih SR, Tsay HJ, Li HC, Greengard P, and Nairn AC (1999). Characterization of the inhibition of protein phosphatase-1 by DARPP-32 and inhibitor-2. J. Biol. Chem. 274, 7870–7878. 10.1074/jbc.274.12.7870. [PubMed: 10075680]
38. Nasa I, Rusin SF, Kettenbach AN, and Moorhead GB (2018). Aurora B opposes PP1 function in mitosis by phosphorylating the conserved PP1-binding RVxF motif in PP1 regulatory proteins. Sci. Signal. 11, eaai8669. 10.1126/scisignal.aai8669. [PubMed: 29764992]
39. Vagnarelli P, Ribeiro S, Sennels L, Sanchez-Pulido L, de Lima Alves F, Verheyen T, Kelly DA, Ponting CP, Rappsilber J, and Earnshaw WC (2011). Repo-Man coordinates chromosomal reorganization with nuclear envelope reassembly during mitotic exit. Dev. Cell 21, 328–342. 10.1016/j.devcel.2011.06.020. [PubMed: 21820363]
40. Hornbeck PV, Chabra I, Kornhauser JM, Skrzypek E, and Zhang B (2004). PhosphoSite: a bioinformatics resource dedicated to physiological protein phosphorylation. Proteomics 4, 1551–1561. 10.1002/pmic.200300772. [PubMed: 15174125]
41. Blom N, Gammeltoft S, and Brunak S (1999). Sequence and structure-based prediction of eukaryotic protein phosphorylation sites. J. Mol. Biol. 294, 1351–1362. 10.1006/jmbi.1999.3310. [PubMed: 10600390]
42. Choy MS, Page R, and Peti W (2012). Regulation of protein phosphatase 1 by intrinsically disordered proteins. Biochem. Soc. Trans. 40, 969–974. 10.1042/BST20120094. [PubMed: 22988849]
43. Bollen M, Peti W, Ragusa MJ, and Beullens M (2010). The extended PP1 toolkit: designed to create specificity. Trends Biochem. Sci. 35, 450–458. 10.1016/j.tibs.2010.03.002. [PubMed: 20399103]
44. Brauer BL, Moon TM, Sheftic SR, Nasa I, Page R, Peti W, and Kettenbach AN (2019). Leveraging new definitions of the LxVP SLiM to discover novel calcineurin regulators and substrates. ACS Chem. Biol. 14, 2672–2682. 10.1021/acschembio.9b00606. [PubMed: 31633908]
45. Kliche J, and Ivarsson Y (2022). Orchestrating serine/threonine phosphorylation and elucidating downstream effects by short linear motifs. Biochem. J. 479, 1–22. 10.1042/BCJ20200714. [PubMed: 34989786]
46. Lee W, Tonelli M, and Markley JL (2015). NMRFAM-SPARKY: enhanced software for biomolecular NMR spectroscopy. Bioinformatics 31, 1325–1327. 10.1093/bioinformatics/btu830. [PubMed: 25505092]
47. Zwart PH, Afonine PV, Grosse-Kunstleve RW, Hung L-W, Ioerger TR, McCoy AJ, McKee E, Moriarty NW, Read RJ, Sacchettini JC, et al. (2008). Automated structure solution with the PHENIX suite. Methods Mol. Biol. 426, 419–435. 10.1007/978-1-60327-058-8_28. [PubMed: 18542881]
48. Emsley P, Lohkamp B, Scott WG, and Cowtan K (2010). Features and development of Coot. Acta Crystallogr. D Biol. Crystallogr. 66, 486–501. 10.1107/S0907444910007493. [PubMed: 20383002]
49. Scheuermann TH, and Brautigam CA (2015). High-precision, automated integration of multiple isothermal titration calorimetric thermograms: new features of NITPIC. Methods 76, 87–98. 10.1016/j.ymeth.2014.11.024. [PubMed: 25524420]
50. Zhao H, Piszczek G, and Schuck P (2015). SEDPHAT – a platform for global ITC analysis and global multi-method analysis of molecular interactions. Methods 76, 137–148. 10.1016/j.ymeth.2014.11.012. [PubMed: 25477226]

51. Kelker MS, Page R, and Peti W (2009). Crystal structures of protein phosphatase-1 bound to nodularin-R and tautomycin: a novel scaffold for structure-based drug design of serine/threonine phosphatase inhibitors. J. Mol. Biol. 385, 11–21. 10.1016/j.jmb.2008.10.053. [PubMed: 18992256]

52. Peti W, Nairn AC, and Page R (2013). Structural basis for protein phosphatase 1 regulation and specificity. FEBS J. 280, 596–611. 10.1111/j.1742-4658.2012.08509.x. [PubMed: 22284538]

53. Pothineni SB, Venugopalan N, Ogata CM, Hilgart MC, Stepanov S, Sanishvili R, Becker M, Winter G, Sauter NK, Smith JL, and Fischetti RF (2014). Tightly integrated single- and multi-crystal data collection strategy calculation and parallelized data processing in JBluIce beamline control system. J. Appl. Crystallogr. 47, 1992–1999. 10.1107/S1600576714022730. [PubMed: 25484844]

54. Prévost M, Chamousset D, Nasa I, Freele E, Morrice N, Moorhead G, and Trinkle-Mulcahy L (2013). Quantitative fragmentome mapping reveals novel, domain-specific partners for the modular protein RepoMan (recruits PP1 onto mitotic chromatin at anaphase). Mol. Cell. Proteomics 12, 1468–1486. 10.1074/mcp.M112.023291. [PubMed: 23362328]

55. Dundr M, Ospina JK, Sung M-H, John S, Upender M, Ried T, Hager GL, and Matera AG (2007). Actin-dependent intranuclear repositioning of an active gene locus in vivo. J. Cell Biol. 179, 1095–1103. 10.1083/jcb.200710058. [PubMed: 18070915]

Highlights

- The RRP1B:PP1 complex highlights an unusual PP1 holoenzyme structure
- RRP1B engages PP1 using both canonical and atypical SLiM interactions
- The isoform selectivity of RRP1B for PP1β/γ is determined by a single amino acid
- RRP1B phosphorylation outside the RVxF SLiM inhibits PP1 recruitment and binding

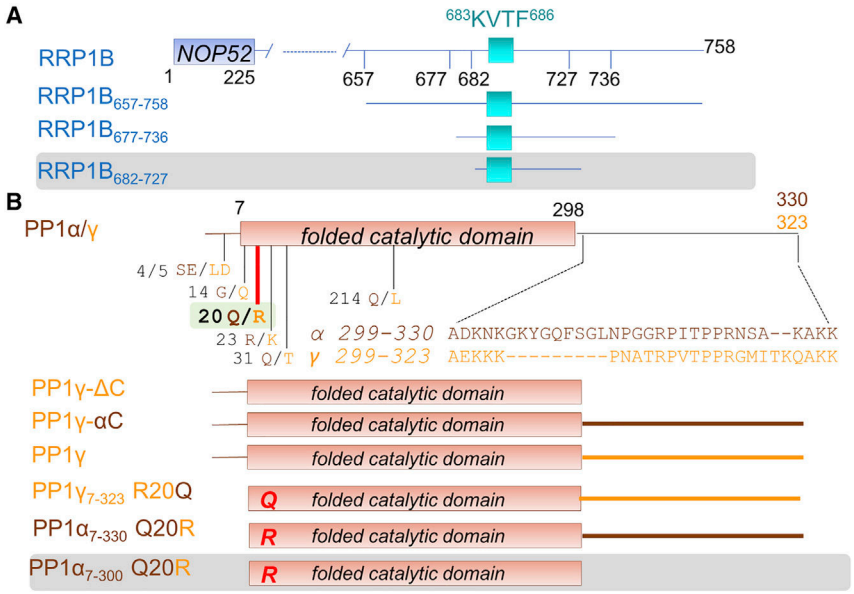

Figure 1. RRP1B and PP1 constructs

(A) Domain structure of RRP1B. Folded RRP1 domain and PP1-specific RVxF SLiM (KVTF) are indicated. Constructs used in this study are illustrated.

(B) Isoform differences between PP1α and PP1γ. Constructs used for RRP1B:PP1 holoenzyme crystal formation are boxed in gray.

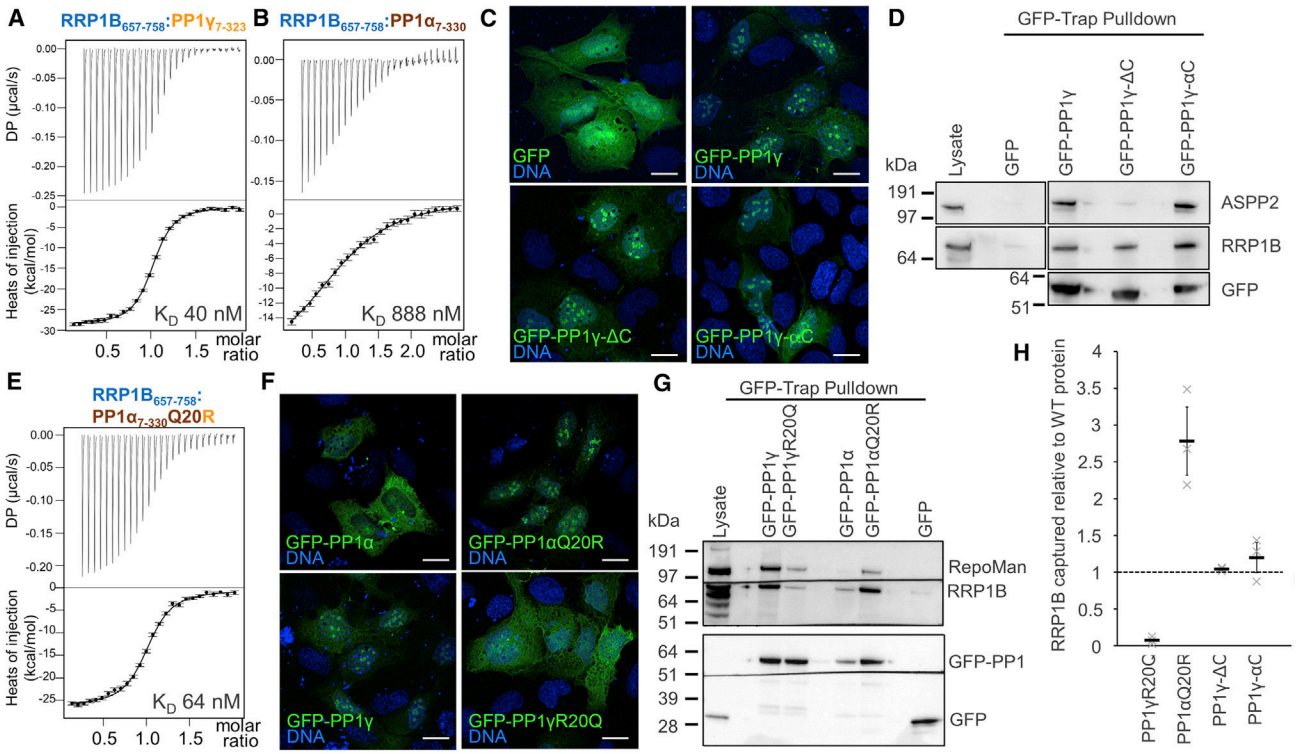

Figure 2. Interaction of RRP1B with PP1 isoforms

(A and B) ITC thermograms of $RRP1B_{657–758}$ with PP1γ (A) or PP1α (B).

(C) Localization of GFP and GFP-PP1γ constructs in live U2OS cells counterstained with the permeable DNA dye Hoechst 33342 (representative images from three biological replicates). Scale bars, 5 μm.

(D) Western blot analysis of co-precipitation of ASPP2 and RRP1B with GFP and GFP-PP1γ constructs captured on GFP-Trap_A beads.

(E) ITC thermogram of $RRP1B_{657–758}$ with $PP1α_{7–330}$ Q20R.

(F) Localization of GFP-PP1α, GFP-PP1γ, GFP-PP1α Q20R, and GFP-PP1γ R20Q constructs in live U2OS cells counterstained with the permeable DNA dye Hoechst 33342 (representative images from three biological replicates). Scale bars, 5 μm.

(G) Western blot analysis of co-precipitation of RepoMan and RRP1B with GFP, GFP-PP1α, GFP-PP1γ, GFP-PP1α Q20R, and GFP-PP1γ R20Q constructs captured on GFP-Trap_A beads.

(H) Quantification of RRP1B co-precipitated by the indicated PP1 variants (D and G), relative to WT (mean ± SE, n ≥ 3). For each experiment, Image Lab software was used to quantify the RRP1B signal per GFP signal.

See also Table S1 and Figure S1.

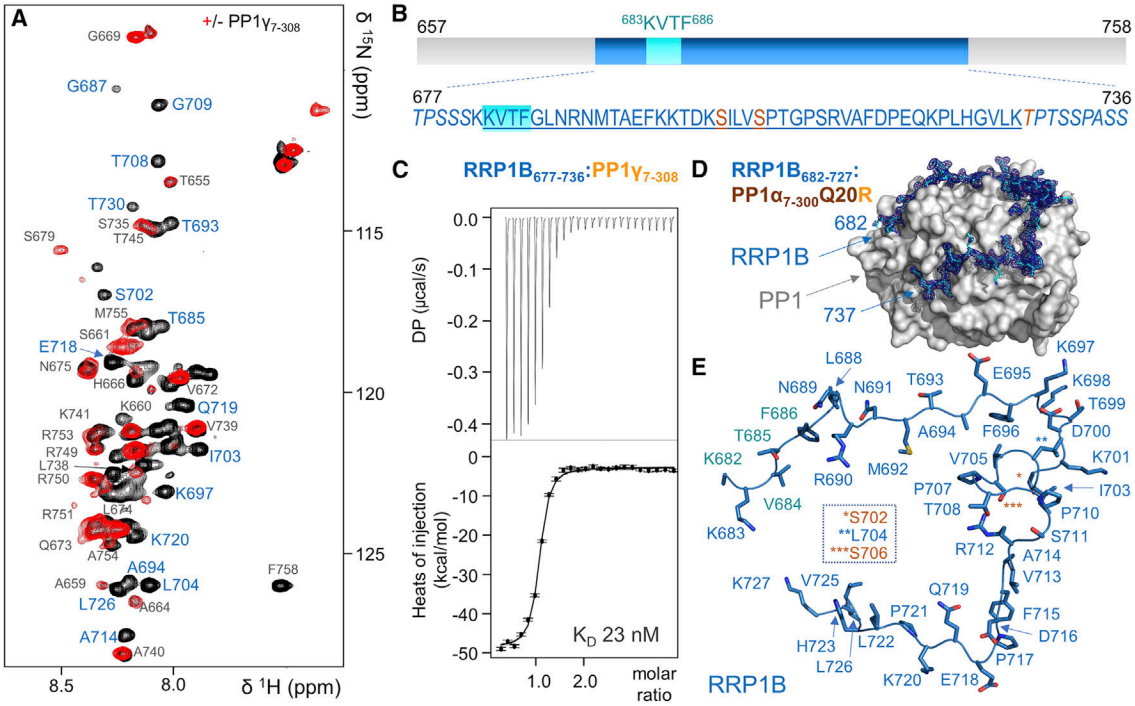

Figure 3. The RRP1B:PP1 holoenzyme

(A) Two-dimensional [^{1}H,^{15}N] HSQC spectrum of ^{15}N-labeled RRP1B$_{657–758}$ alone (black) and in complex with PP1$\gamma_{7–308}$.

(B) Identification of all RRP1B residues that interact with PP1 to identify the core RRP1B PP1-binding domain.

(C) ITC thermograms of RRP1B$_{677–736}$ with PP1$\gamma_{7–308}$.

(D) Crystal structure of the RRP1B:PP1$\alpha_{7–300}$ Q20R holoenzyme. PP1 is in gray and RRP1B$_{682–727}$ is in cyan with the 2mF_o-DF_c electron density map contoured at 1σ (1.8 Å); first and last RRP1B residues visible in the electron density map are indicated.

(E) Structure of RRP1B$_{682–727}$ when bound to PP1.

See also Tables S1 and S2 and Figure S2.

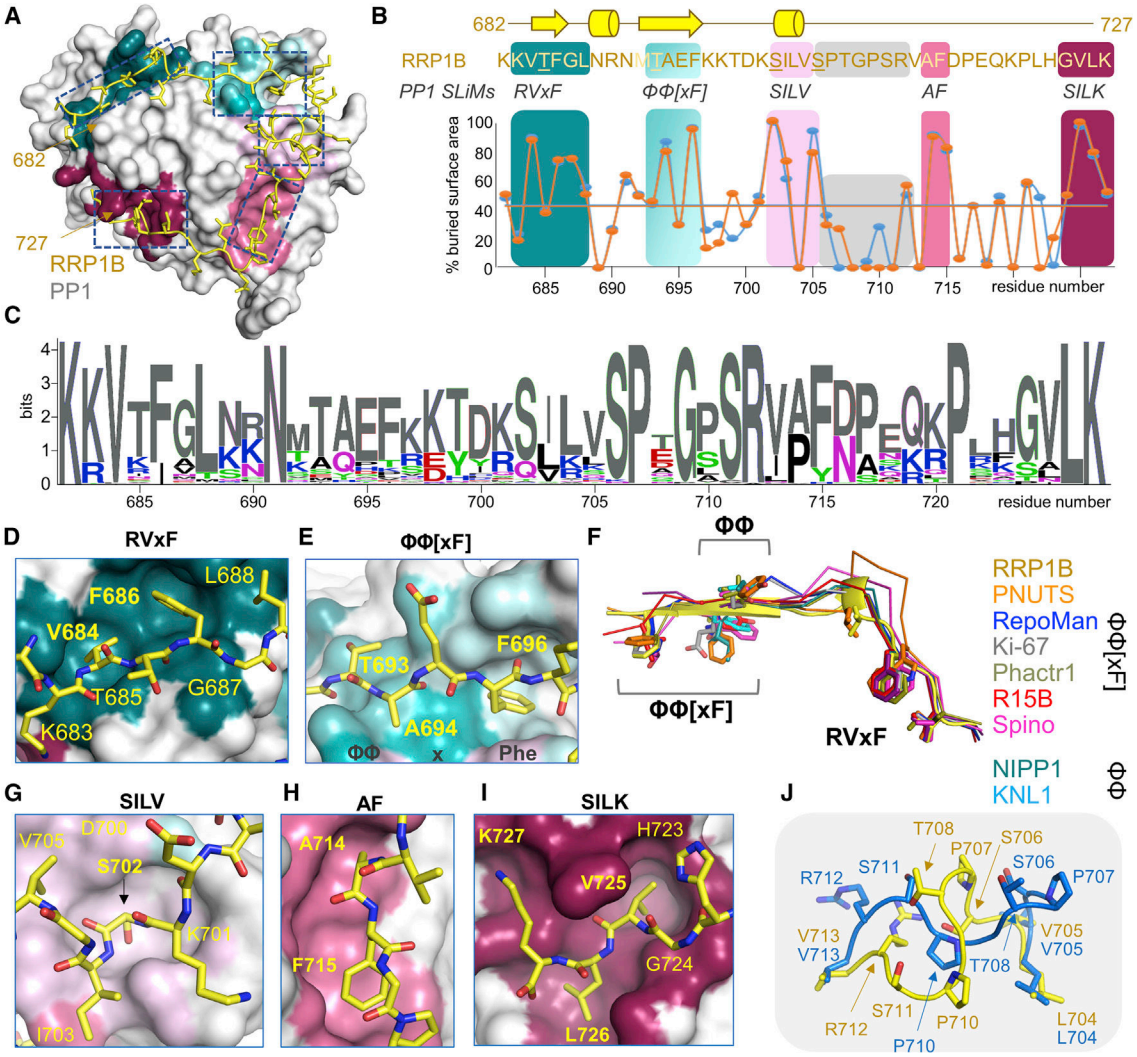

Figure 4. RRP1B binds PP1 via multiple interaction surfaces

(A) Crystal structure of the RRP1B$_{682–727}$:^{Q20R}PP1α$_{7–300}$ complex. RRP1B is shown as yellow sticks with PP1 shown as a gray surface. PP1 SLiM binding pockets to which RRP1B binds (RVxF, ΦΦ[xF], SILV, AF, SILK) are colored from teal to coral. Dashed boxes correspond to the zoomed-in pockets shown in (D), (E), (G), (H), and (I).

(B) Upper: RRP1B sequence with secondary structure (top) and SLiM motifs (bottom) indicated. Lower: percentage of buried surface area plotted by residue for each RRP1B chain (two complexes were present in the asymmetric unit). Shaded areas correspond to RRP1B residues that bind in PP1 SLiM binding pockets and colored according to shaded pockets in (A). Gray shaded box highlights RRP1B residues that adopt distinct conformations in the two complexes.

(C) Sequence logo of RRP1B sequences from 319 distinct species; sequence crystallized is colored gray.

(D and E) Major binding interactions between RRP1B (yellow sticks) and PP1 (surface), colored as in (A). The well-established SLiM binding pockets (D, RVxF; E, ΦΦ[xF]) are shown.

(F) Overlay of the RVxF and ΦΦ[xF] structures from nine PP1 holoenzymes, with residues binding RVxF, ΦΦ, and ΦΦ[xF] pockets shown as sticks.
(G–I) SILV (L704 sidechain not shown for clarity, G), AF (H), and SILK (I) binding pockets with RRP1B (yellow sticks) and PP1 (surface), colored as in (A).
(J) Both RRP1B:PP1 complexes present in the asymmetric unit overlaid using PP1; the distinct RRP1B chains are colored yellow and blue.

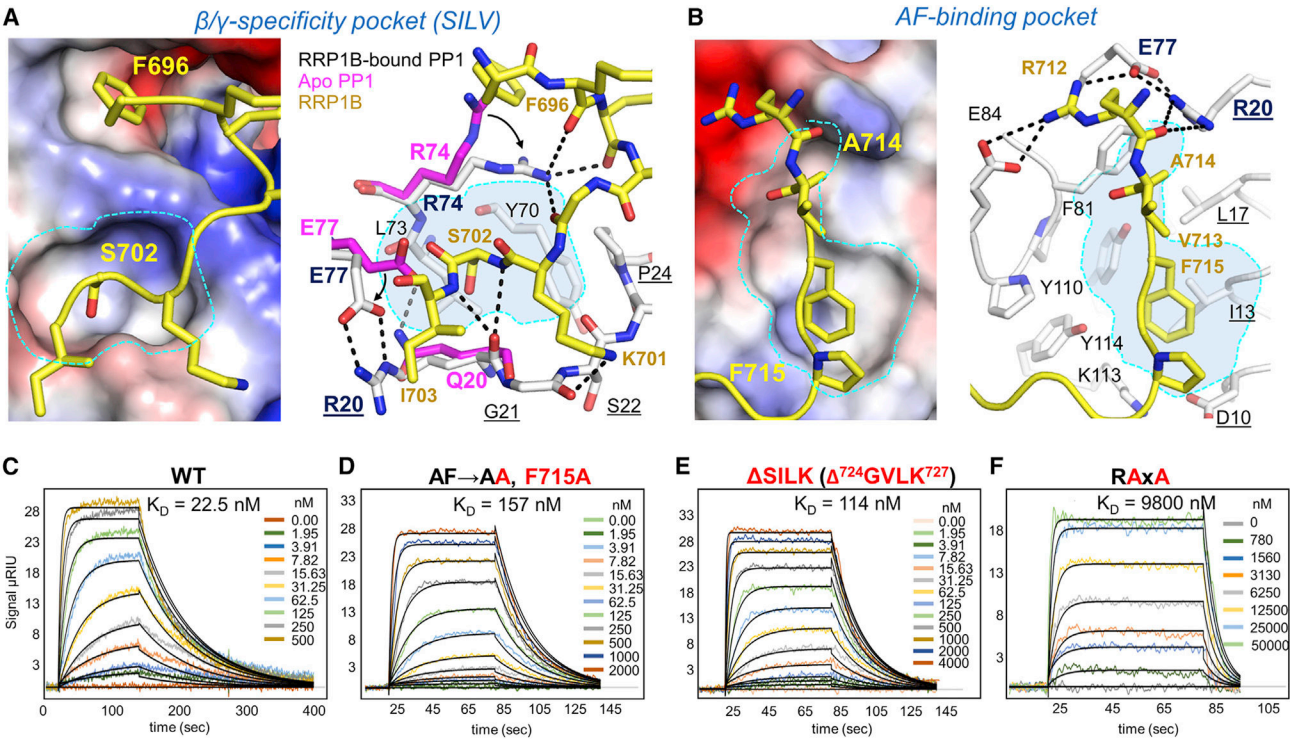

Figure 5. Non-canonical regulator interaction sites on PP1

(A) The Arg20 β/γ-specificity pocket. Left; PP1α Q20R is shown as an electrostatic surface while RRP1B (yellow) is shown as a ribbon with a subset of side chains, including Ser702, shown as sticks. Arg20 β/γ-specificity pocket is highlighted by a dashed line (cyan). Right: same view, but with PP1 (white, RRP1B-bound PP1; magenta, free PP1) and RRP1B (yellow) shown as sticks. Hydrogen bonds/salt bridges are shown as black dashed lines. Arrows highlight the rotations of PP1 Arg74 and Glu77 that occur upon RRP1B binding. The location of the Arg20 β/γ-specificity pocket is indicated in gray with a cyan dashed line. PP1 residues underlined correspond to the PP1 N-terminal loop.

(B) The N-terminal binding groove. Left: PP1 is shown as an electrostatic surface while RRP1B (yellow) is shown as a ribbon with a subset of side chains, including Ser702, shown as sticks. The N-terminal groove is highlighted by a dashed line (cyan). Right: same view, but with PP1 (white) and RRP1B (yellow) shown as sticks. Hydrogen bonds/salt bridges are shown as black dashed lines. The location of the N-terminal binding groove is indicated in gray with a cyan dashed line. PP1 residues underlined correspond to the PP1 helix α1.

(C–E) SPR sensorgrams between RRP1B (WT and variants) and PP1α$_{7–330}$ Q20R.

(C) WT RRP1B$_{682–727}$, (D) RRP1B$_{682–727}$ F715A, (E) ΔSILK: RRP1B$_{682–723}$, and (F) RRP1B$_{682–727}$ KATA (RAxA mutant).

See also Table S3.

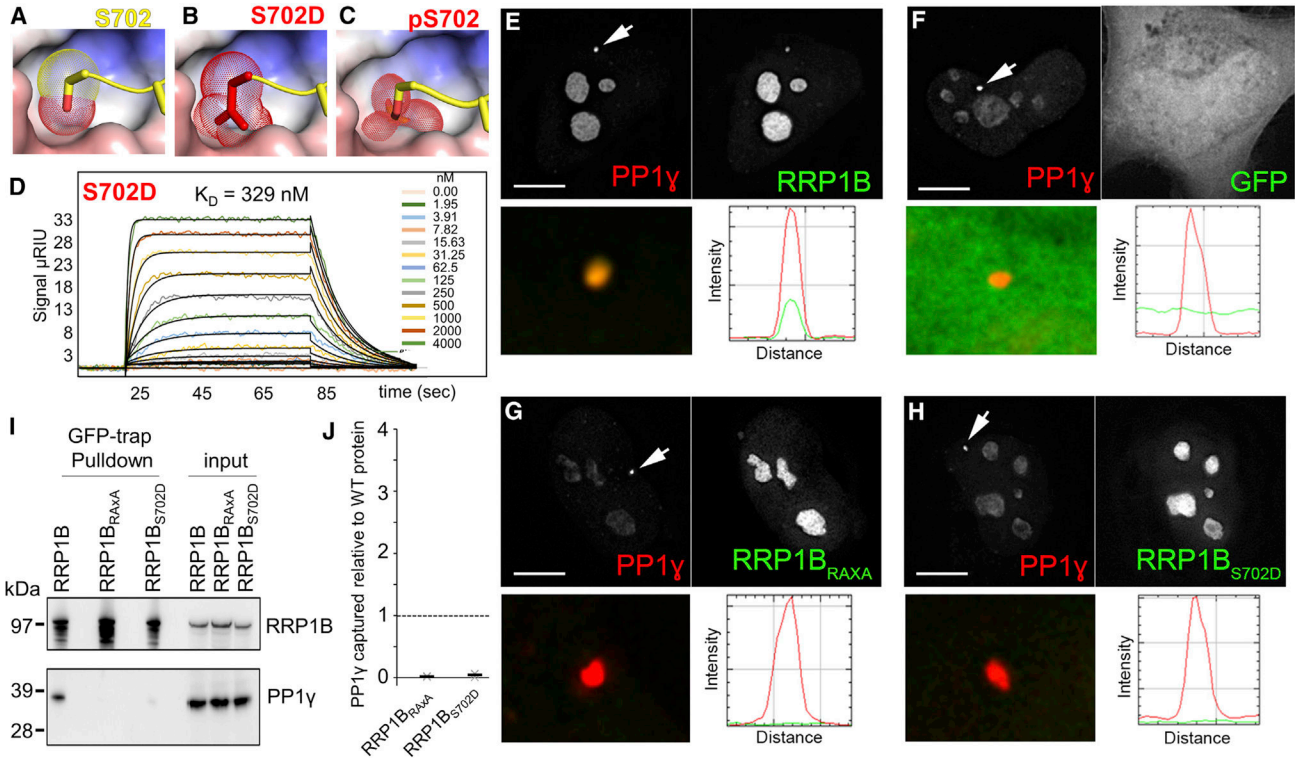

Figure 6. RRP1B phosphorylation weakens PP1 binding

(A–C) The Arg20 β/γ-specificity pocket with the PP1 surface colored by electrostatics and RRP1B (A: Ser702) or modeled RRP1B variants (B: S702D; C: pSer702) shown as sticks (yellow); side-chain atoms are shown as dots to illustrate their space-filling volume.

(D) SPR sensorgram between $RRP1B_{S702D}$ and $PP1\alpha_{7–330}$ Q20R.

(E–H) HeLa/TetU2 cells with stably integrated 256xLacO repeats transiently transfected with pmCherry-LacR-NLS-PP1γ and either GFP-RRP1B WT (E), GFP alone (F), GFP-$RRP1B_{RAxA}$ (G), or GFP-$RRP1B_{S702D}$ (H). In four biological replicates (representative images shown here), GFP-RRP1B WT accumulated at the gene locus in 98% ± 2% of 120 cells scored, GFP alone and GFP-$RRP1B_{RAxA}$ in 0% of 120 cells scored, and GFP-RRP1B S702D in 7% ± 2% of 120 cells scored. Graphs illustrate plot line profiles for red and green fluorescence intensity over 2 µm at the gene locus. Scale bars, 5 µm.

(I) Western blot analysis of co-precipitation of PP1γ from U2OS cells with GFP-RRP1B, GFP-$RRP1B_{RAxA}$, and GFP-$RRP1B_{S702D}$ (representative blot from three biological replicates).

(J) Quantification of PP1γ co-precipitated by the indicated RRP1B variants (I), relative to WT GFP-RRP1B (mean ± SE; n ≥ 3). For each experiment, Image Lab software was used to quantify the PP1γ signal per GFP signal. The amount of PP1γ pulled down by GFP-$RRP1B_{RAxA}$ is 2.1% ± 0.6% and that of GFP-$RRP1B_{S702D}$ is 4.6% ± 2.0% compared with GFP-RRP1B WT.

See also Tables S3 and S4 and Figure S3.

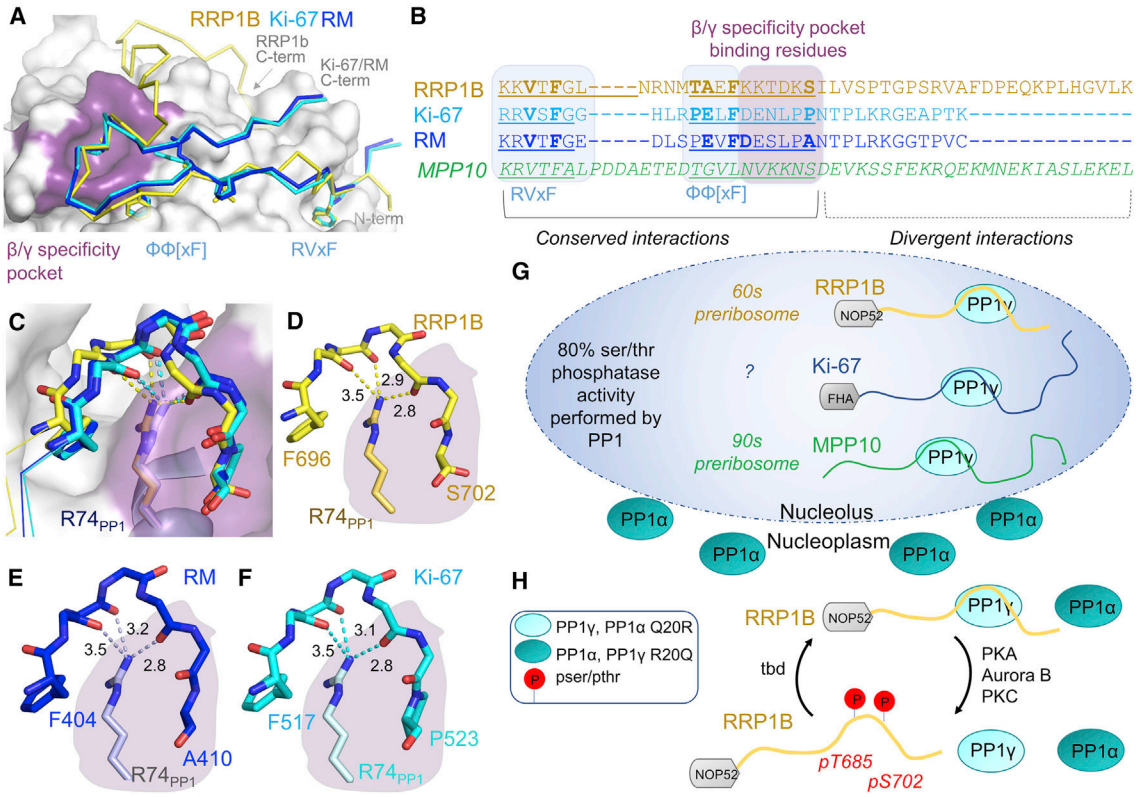

Figure 7. IDP regulators that are specific for PP1β/PP1γ bind the β/γ-specificity pocket

(A) Overlap of the RRP1B:PP1, Ki-67:PP1, and RepoMan (RM):PP1 complexes. RRP1B (yellow), Ki-67 (cyan), and RM (blue) are shown as ribbons with PP1 shown as a gray surface. The β/γ-specificity pocket is magenta. Side chains that bind the major interaction pockets are shown as sticks.

(B) Structure-based sequence alignment of the PP1 interaction domains of RRP1B, Ki-67, and RM, with PP1 interacting residues indicated. Underlined residues have identical conformations.

(C) Close-up view of the interactions stabilizing the loops between the [xF] Phe residue and the β/γ-specificity pocket binding residue. Regulators are colored as in (A) and shown as sticks. Side chains are shown for the Phe and β/γ-specificity pocket binding residue.

(D–F) Same view as (C), but on the RRP1B:PP1 (D), RM:PP1 (E), or Ki-67:PP1 (F) complexes. Hydrogen bonds are indicated by dashed lines, with the distances in angstroms.

(G) Cartoon highlighting the major regulators of PP1γ in the nucleolus.

(H) RRP1B:PP1 holoenzyme assembly is regulated by phosphorylation on a least two residues, Thr685 (the “x” residue in the RRP1B RVxF motif) and Ser702. Potential kinases are indicated (phosphosite3.1);[40] the reversing phosphatases are unknown.

KEY RESOURCES TABLE

REAGENT or RESOURCE	SOURCE	IDENTIFIER
Antibodies		
Anti-RRP1b antibody	Abcam	Cat #ab224105
Anti-CDCA2 antibody	Abcam	Cat #ab45129, RRID AB_869084
Anti-53BP2/ASPP2/BBP antibody	Abcam	Cat #ab181377
GFP antibody [PABG1]	Chromotek	Cat #PABG1-100, RRID AB_274847
Goat anti-rabbit IgG (H + L), HRP-conjugated	ThermoFisher	Cat #31460, RRID AB_228341
Anti-PP1γ antibody	Santa Cruz	Cat# sc-515943, RRID AB_2909495
Bacterial and virus strains		
E.coli BL21 (DE3) GOLD expression strain	Agilent	Cat #230132
E.coli GOLD alpha select competent cells	Bioline	Cat #BIO-85027
Chemicals, peptides, and recombinant proteins		
pGro 7 Chaperone	Takara	Cat #3340
QuikChange site-directed mutagenesis kit	Agilent	Cat # 200524
GeneArt Gibson Assembly HiFi cloning kit	ThermoFisher	Cat #A46624
^{15}N ammonium chloride 99%	Cambridge Isotope Laboratories	Cat #NLM-465-25
D-Glucose (U-^{13} C6, 99%)	Cambridge Isotope Laboratories	Cat #CLM-1396-25
D_2O	Sigma	Cat #B6891
β-D-thiogalactopyranoside (IPTG)	Gold Bio	Cat #367-93-1
Tween 20	Fisher	Cat #BP337-500
Triton X-100	Fisher	Cat #BP151-500
Complete Protease inhibitor tablets	Roche	Cat #14696200
Kanamycin	Gold Bio	Cat #K-120-100
Tris (2-carboxyethyl) phosphine hydrochloride (TCEP)	Gold Bio	Cat #TCEP-25
Ni Sepharose 6 Fast flow 1000mL	GE Healthcare	Cat #17-5318-04
HiLoad 26/60 Superdex 75 pg	GE Healthcare	Cat #17-1070-01
HiLoad 26/60 Superdex 200 pg	GE Healthcare	Cat #28-9893-36
PEG 8000	Hampton Research	Cat #HR2-535
Morpheus screen	Molecular Dimensions	Cat #MD1-46
Ni-NTA functionalized polycarboxylate (NiHC200M) SPR chip	XanTec Bioanalytics GmbH	Cat #SCR NiHC200M
Dulbecco's modified Eagles' medium (DMEM)	Wisent Bioproducts Inc	Cat #319-062-CL
Pierce BCA Protein Assay kit	ThermoFisher	Cat #23225
AccuOrangeTM Protein Quantification Kit	Biotium	Cat #30071-T
Phenol Red-free CO_2 independent medium	ThermoFisher	Cat #18045088
bisBenzimide H 33,342 trihydrochloride (Hoechst 33,342)	Millipore Sigma	Cat #B2261
PEI (Polyethylenimine)	Polysciences Inc.	Cat #23966

REAGENT or RESOURCE	SOURCE	IDENTIFIER
GFP-Trap A beads	Chromotek	Cat #gta-100
NuPAGE 4–12% BisTris gel	ThermoFisher	Cat # NP0326BOX
Deposited data		
BMRB (NMR assignment of RRP1b$_{657–758}$)	This study	BMRB ID: 51132
PDB (Structure of PP1α7-300^{Q20R}:RRP1b$_{682–727}$)	This study	PDB ID: 7T0Y
Experimental models: Cell lines		
U-2 OS cells (human osteosarcoma epithelial; female-derived)	ATCC	Cat #ATCC® HTB-96™ RRID:CVCL_0042
Recombinant DNA		
pRP1B-Thio$_6$-His$_6$-TEV-PP1γ 7–323	Addgene	ID 51770
pRP1B-Thio$_6$-His$_6$-TEV-PP1α 7–330	Addgene	ID 51768
pRP1B-Thio$_6$-His$_6$-TEV-PP1α 7–300	Addgene	ID 26566
pRP1B-Thio$_6$-His$_6$-TEV-PP1γ 7–308	Peti Laboratory	Available on request
pRP1B-Thio$_6$-His$_6$-TEV-PP1α 7–330 Q20R	Peti Laboratory	Available on request
pRP1B-Thio$_6$-His$_6$-TEV-PP1α 7–300 Q20R	This study	Available on request
pJ411 Thio$_6$-His$_6$-TEV-RRP1b$_{657–758}$	This study/DNA 2.0	Available on request
pET-M30-MBP-TEV-RRP1b$_{677–736}$	This study	Available on request
pET-M30-MBP-TEV-RRP1b$_{682–727}$	This study	Available on request
pET-M30-MBP-TEV-RRP1b$_{682–727}$ S702D	This study	Available on request
pET-M30-MBP-TEV-RRP1b$_{682–727}$ F715A	This study	Available on request
pET-M30-MBP-TEV-RRP1b$_{682–727}$ KVTF-KATA	This study	Available on request
pET-M30-MBP-TEV-RRP1b$_{682–723}$ ΔGVLK	This study	Available on request
pEGFP(C1)-PP1α	Addgene	ID 44224
pEGFP(C1)-PP1γ	Addgene	ID 44225
pEGFP(C1)-PP1γΔ299–323	This study	Available on request
pEGFP(C1)-PP1γ(1–298)PP1α(299–330)	This study	Available on request
pEGFP(C1)-PP1α (Q20R)	This study	Available on request
pEGFP(C1)-PP1γ(R20Q)	This study	Available on request
pEGFP(C1)-RRP1B	This study	Available on request
pEGFP(V1)-RRP1B(V684A/F686A)	This study	Available on request
pEGFP(C1)-RRP1B(S702D)	This study	Available upon request
Software and algorithms		
Topspin 2.0/3.0/3.1	Bruker	https://www.bruker.com
CARA	www.cara.nmr.ch	www.cara.nmr.ch
NMRFAM-Sparky	Lee, W et al. (2015)[46]	https://nmrfam.wisc.edu/nmrfam-sparky-distribution/
PHENIX	Zwart et al., (2008)[47]	https://www.phenix-online.org/

REAGENT or RESOURCE	SOURCE	IDENTIFIER
COOT	Emsley et al., (2010)[48]	https://www2.mrc-lmb.cam.ac.uk/personal/pemsley/coot/
Pymol	Schrodinger, LLC	https://www.pymol.org
NITPIC	Scheuermann et al., (2015)[49]	https://www.utsouthwestern.edu/labs/mbr/software/
SEDPHAT	Zhao et al., (2015)[50]	https://www.utsouthwestern.edu/labs/mbr/software/
GUSSI	Scheuermann et al., (2015)[49]	https://www.utsouthwestern.edu/labs/mbr/software/
SoftWorX	GE Healthcare	https://www.directindustry.com/prod/applied-precision/product-20760-405306.html
Image Lab software	Biorad	https://www.bio-rad.com/en-in/product/image-lab-software?ID=KRE6P5E8Z
SPR Autolink 4 Channel	Reichert	https://www.reichertspr.com/
TraceDrawer	Ridgeview Instruments	https://tracedrawer.com/
Other		
PDB Search model	Choy et al., (2014)[10]	PDB ID: 4MOV